ELSEVIER

Contents lists available at ScienceDirect

International Journal of Fatigue

journal homepage: www.elsevier.com/locate/ijfatigue



Steel railway bridge fatigue damage detection using numerical models and machine learning: Mitigating influence of modeling uncertainty



Ahmed Rageh*, Saeed Eftekhar Azam, Daniel G. Linzell

University of Nebraska-Lincoln, Lincoln, NE, USA

ARTICLE INFO

Keywords:
Railway
Bridge
Fatigue
Stringer
Floor beam
Connections
Modeling
Uncertainties
Proper orthogonal decomposition
Artificial neural networks
Damage
Detection

ABSTRACT

Stringer-to-floor beam connections were reported as one of the most fatigue-prone details in riveted steel railway bridges. To detect stiffness degradation that results from the initiation and growth of fatigue cracks, an automated damage detection framework was proposed by the authors (Eftekhar Azam et al., 2019; Rageh et al., 2018). The proposed method relies on Proper Orthogonal Decomposition (POD) and Artificial Neural Networks (ANNs) to identify damage location and intensity under non-stationary, unknown train loads. Bridge computational models were used to simulate damage scenarios and for training the ANNs. Damage detection method efficiency and accuracy were shown to be significantly influenced by the level of modeling uncertainties (MUs). To investigate the applicability of the proposed framework to in-service bridges, a systematic analysis of the effect of MUs on the proposed POD-ANN framework was necessary. MU influence on the performance of the POD-ANN damage detection method was investigated and a new procedure for generating training data for ANNs was proposed. The procedure was based on synergizing Proper Orthogonal Modes (POMs) extracted from measured structural response and POMs calculated from the numerical model. The current study integrated numerical and field investigations. The main objective of the numerical investigation was to identify a robust damage feature independent of the level and location of assumed MUs. Results showed that Damage Location (DL) and Damage Intensity (DI) were detected with high accuracy for studied uncertainty cases; however, as expected, damage detection accuracy reduced as MU increased. A hybrid experimental-numerical approach was then implemented for the field investigation studies. This approach applied identified damage features from the numerical investigation to measurements from an in-service railway bridge to produce damage scenarios used to train the framework. MATLAB algorithms were developed that preprocessed field data and eliminated POM variations resulted from loading uncertainties. ANNs were trained and tested using the field strain estimated POMs from the hybrid approach and DL and DI results were obtained for the studied railway bridge under nonstationary, unknown train loads. These results show the promise of the POD-ANN method as a robust, real-time fatigue damage identification tool for steel railway bridges.

1. Introduction

Over 60% of railway bridges were constructed before 1950, with 50% of those structures being steel bridges that generally used riveted connections [3]. In general, steel bridges are subjected to a wide range of deficiencies associated with fatigue and corrosion [4]. Specifically, common structural deficiencies in steel railway bridges include deterioration of stringer-to-floor beam and stringer-to-lower lateral bracing connections and frozen bearings [5]. Bridge owners are certainly concerned about all these deficiencies; however, stringer-to-floor beam connection deterioration is of significant importance for these type of bridges as connection failure could cause extensive damage and

possibly failure, leading to safety concerns and traffic disruptions [4,6,7]. As a result, the current study focuses on the identification of these types of deficiencies.

The behavior and integrity of riveted steel railway bridges have been examined by multiple investigators. A railway deck truss was examined and interaction between various bridge elements was shown to induce additional internal effects, such as stringer axial forces and floor beam lateral bending, due to main truss longitudinal deformations [8]. Consequently, the fatigue life of those components and their connections might be compromised. Published numerical and laboratory research concluded that stringer-to-floor beam connections are more rigid than they initially assumed and, as a result, large bending stress

E-mail address: a.eissa.rageh@huskers.unl.edu (A. Rageh).

^{*} Corresponding author.

Nomenclature		$\widehat{oldsymbol{arphi}}_{exp}^d \ oldsymbol{arphi}$	estimated damage scenario φ for field measurements proper orthogonal decomposition 1st mode (POM 1)
List of symbols and	acronyms	$oldsymbol{arphi}_{M_i}^h \ oldsymbol{arphi}_{M_i}^d$	healthy scenario φ for modeling uncertainty case i damage scenario φ for modeling uncertainty case i
POD proper of POMs proper of ANNs artificial IL instrume DL simulate DI simulate MU modelin	al health monitoring orthogonal decomposition orthogonal decomposition modes I neural networks ented location ed damage location ed damage intensity g uncertainty ng uncertainty case (i = 0-5)	$oldsymbol{arphi}_{-M_i}^{M_i} oldsymbol{arphi}_{e^{ ext{cxp}}}^{d} oldsymbol{arphi}_{e^{ ext{cxp}}} oldsymbol{\Delta arphi}_{-M_i} oldsymbol{\Delta arphi}_{-M_i} oldsymbol{arphi}_{e^{ ext{cxp}}} oldsymbol{\widehat{arphi}}_{d^{ ext{d}}_i}^{d}$	healthy scenario φ for field measurements damage scenario φ for field measurements difference between φ of a damage scenario and φ of a healthy scenario under the same load $\Delta \varphi$ for modeling uncertainty case i $\Delta \varphi$ for field measurements estimated damage scenario φ for modeling uncertainty case i

cycles and corresponding fatigue degradation in connecting angles and rivets may develop [4,6–12]. An analytical study focused on stringer end fixity ratio effects on fatigue damage accumulation found that stringer-to-floor beam connections experienced more severe damage than floor beam-to-main girder connections in steel riveted plate girder railway bridges [10]. Another study showed that, for double-track steel railway bridges, increased connection fatigue damage was observed when both tracks were loaded simultaneously [6]. A full-scale laboratory test on three panels from a demolished riveted steel railway bridge concluded that stringer ends could be subjected to negative end moments that were 67% of continuous stringer bending moments and vertical fatigue cracks developed in connecting angles under cyclic loading [7].

Bridge condition is commonly assessed using visual inspections at a prescribed frequency, a process that is qualitative, costly, and possibly unsafe [13]. Developing an efficient, automated Structural Health Monitoring (SHM) approach that continuously reports bridge health under various loading and environmental situations is strongly desired to track short and long-term changes in condition and ensure safety [14]. SHM systems, which extract information via processing measured responses and apply damage identification methods to the data to extract important information, are usually data-driven and incorporate sparse sensor networks to collect desired response quantities such as strains, accelerations or displacements [15]. A considerable amount of research effort has been dedicated to investigating key aspects associated with the development of data-driven SHM systems that can identify fatigue prone regions and detect damage. For example, studies have been completed that investigate the effectiveness of fiber optic sensors for fatigue damage detection and their use within SHM systems [16-18]. The influence of material degradation on dynamic characteristics, including modal curvature [19] and strain energy [20,21] and resulting Eigenmodes [22,23], has also been investigated.

Other research has focused on improving numerical techniques used to identify the damage, such as one study that implemented Principle Component Analysis to utilize frequency variations as damage indicators, independent of site conditions [24]. Laboratory tests of a short, based-excited cantilevered beam were completed at twelve temperatures with "damage" represented as changes in mass. PCA was shown to detect these "damage" levels successfully. Analytical studies were also performed and showed that frequencies were influenced by moving load mass and speed, damage location and intensity [24]. Recently, some researchers have focused on developing a damage localization framework utilizing Proper Orthogonal Decomposition (POD) [25]. In one study, an algorithm that produced POD based on a structure's Frequency Response Function (FRF) was used to detect simulated beam damage, with that damage being effectively detected over a specific frequency range [26,27]. Research focusing on using multiple numerical methods, including Artificial Neural Networks (ANNs), Principle Component Analysis and Radial Basis Functions, to detect wind turbine blade fatigue damage has shown promising results when

compared against experimental studies that induced fatigue cracks [28]. Another study that compared statistical damage features and modal parameters showed that statistically-based methods were more effective at detecting damage [29]. While data-driven methods have been shown to be an efficient tool to detect damage, current literature lacks data from actual, in-service structures needed to further train associated SHM frameworks. Even if a bridge owner allows for the exploration of several damage scenarios in-situ, sufficient data would not be produced to train the framework. To address this issue, work presented herein implements a hybrid experimental-numerical, outputonly approach to develop damage training scenarios under non-stationary excitations. Classical output-only damage detection methods are usually based on the operational modal analysis under stationary excitations and require low signal-to-noise ratios. To include non-stationary loading conditions, the authors developed a damage detection methodology based on POD and ANNs that integrated analytical and experimental data [1,2]. Supervised learning was used to classify output-only response, reduce Proper Orthogonal Mode (POM) variations from load variability and directly associate detected changes caused by variations in Damage Intensity (DI) and Damage Location (DL). Several aforementioned damage identification methods rely on computational models for identification of structural damage; therefore, MU can affect their damage identification precision and robustness.

MUs that influence damage detection effectiveness have been addressed using three SHM frameworks: offline; online; and machine learning [30-36]. Offline framework applications have been examined by multiple researchers, with one study investigating modeling error effects on a model-based framework using a numerical process that involved optimal selection of modes and modal residual weights to define multiple model updating classes [30]. Bayesian model class selection and model averaging techniques were implemented to detect damage for selected classes and structural damage was detected with high accuracy when performed analytically [30]. Another study involved examined modeling error effects on a damage detection framework based on wavelet coefficients developed using finite element (FE) analyses of a two-dimensional (2D) frame under sinusoidal excitation [31]. Simulated errors included excitation force, mass, support stiffness, member bending stiffness and damping ratios and the framework was minimally influenced by the errors [31]. Dynamic tests on a full-scale seven-story reinforced concrete building were conducted to further examine uncertainty effects on the accuracy of well-established damage detection methods in an offline framework [32,33]. Certain modal parameter uncertainties, including modeling errors stemming by mesh density, influenced the level of confidence associated with detected damage. Effects arising from modeling errors associated with nonlinear FE model updating have also been examined, with an Unscented Kalman Filter (UKF) used to estimate examined model parameters and data from dynamically tested buildings, one a two-dimensional steel frame and the other a three-dimensional concrete frame, being used to

investigate uncertainty influence on damage detection accuracy [34]. Results showed that MUs had a significant impact on damage detection using updated FE models[34]. The accuracy of online damage detection frameworks of nonlinear systems having unknown parameters and illdefined numerical models have been investigated using a Bayesian approach and UKFs [35]. Chatzi et al. (2010) investigate model complexity and parameterization effects that introduced uncertainties via comparison against laboratory tests of a nonlinear joint setup and the effectiveness of the proposed method was demonstrated [35]. One study of machine learning damage detection frameworks looked at modal property based damage detection and implemented neural-networks to investigate modeling errors [36]. The study found that mode shape component ratios or differences between those ratios, which are considered to be robust damage features, showed minimum sensitivity to modeling errors. Applicability of the framework was validated via numerical analyses, laboratory tests of a simple beam and field tests of a multi-beam bridge. A companion study incorporated a UKF to estimate FE model parameters and a Linear Kalman Filter (LKF) to estimate simulation errors [37]. A 2D steel frame model was employed to validate the approach and MUs included gravity loads, structure geometry, damping ratios and member inertia and results illustrated that using the proposed framework for model updating allowed for more accurate damage detection [37].

It is recognized that using an integrated approach introduces inherent MUs largely related to model complexity. Previously discussed research focused on the POD-ANN framework developed by the authors [1,2] outlined how the method was developed and examined its effectiveness via comparison to numerical models and one week of measured strains from a monitored, in-situ, steel railway bridge. In the previous research work, the influence of the signal to noise ratio on POD-ANN framework effectiveness was also examined. The investigation incorporated correlated and uncorrelated noise with noise ratios of 10, 15 and 20%. It was observed that the framework was robust to noise and damage was accurately detected and located [1,2].

In this study, the effect of model MUs on the accuracy of the developed POD-ANN damage detection framework was investigated to identify robust modeling features that could be implemented when detecting damage of an in-situ railway bridge. The current research work introduced a hybrid experimental-numerical damage detection framework to detect damages in a real-world application. As outlined in the following sections, a numerical investigation was carried out to identify a robust damage feature largely independent of MU. The identified feature was then used to impose damage scenarios to eight weeks of measured strains to train the ANNs to validate further identified feature robustness to MU.

2. POD-ANN method for damage identification in the presence of $\boldsymbol{\mathsf{M}}\boldsymbol{\mathsf{U}}$

2.1. POD for feature extraction

POD of a set of data is accomplished by obtaining a set of ordered, orthonormal bases and collecting detailed information concerning relevant energy contents. As a result, POD addresses feature extraction by discovering underlying, hidden information in the data and dimensionality reduction by appropriately capturing dynamic system features in the smallest corresponding subspace. The concept of POD was central to the development of various techniques, such as: Principal Component Analysis (PCA), Karhunen–Loève decomposition (KLD), and Singular Value Decomposition (SVD) [38–40]. A detailed discussion of PCA, KLD and SVD commonalities can be found elsewhere [41].

The current study uses data sets comprised of samples taken from time histories of in-situ bridge response to a train passage, with data from each train passage being stored in snapshot matrices. SVD of the snapshot matrix helps to extract damage features [40]:

$$\mathbf{U} = \mathbf{L} \Sigma \mathbf{R}^{\mathrm{T}} \tag{1}$$

where: $\mathbf{U} \in \mathbb{R}^{n_m \times n_s}$ is the snapshot matrix from n_m measurements and n_s samples; $\mathbf{L} \in \mathbb{R}^{n_m \times n_m}$ is an orthonormal matrix whose columns are the left singular vectors of \mathbf{U} ; $\Sigma \in \mathbb{R}^{n_m \times n_s}$ is a diagonal semi-matrix whose components Σ_{ii} are singular values of \mathbf{U} ; and $\mathbf{R} \in \mathbb{R}^{n_s \times n_s}$ is an orthonormal matrix whose columns are the right singular vectors of \mathbf{U} . It is known that the left singular vectors are POMs of the snapshot matrix. It was shown that the first bridge response POMs to train passages (i.e., the first left singular vector of the corresponding snapshot matrices) contain information on intensity and location of damage at the stringer to floor-beam connections. It should be noted that, unlike linear vibration modes, structural response POMs could vary as excitation source changes. Therefore, when POMs are used as damage features, a machine learning algorithm is needed to differentiate variations induced by damage from ones caused by load variations.

2.2. ANN for damage identification

Feedforward ANNs have been extensively studied for structural damage identification. To facilitate autonomous damage identification, a two-layer, feedforward ANN was adopted by several authors for creating a nonlinear mapping between damage indices and features extracted from the structural response [42–44]. This architecture has been proven to precisely approximate arbitrary nonlinear functions, provided that they have sufficient numbers of nodes in their hidden layers [45,46]. Based on these studies, ANN feedforward damage identification models have been constructed based on a linear combination of predetermined nonlinear basis functions $\xi_i(\varphi)$ [47]:

$$\boldsymbol{d}(\boldsymbol{\varphi}, \mathbf{W}) = f\left(\sum_{j=1}^{M} w_j \xi_j(\boldsymbol{\varphi})\right)$$
(2)

where: d is the vector of damage indices; φ is the damage feature; W is the matrix of ANN weights; and f (\blacksquare)is the identity for regression problems and is a nonlinear activation function (i.e., softmax). It was proven that this architecture approximated arbitrary nonlinear functions well [46,48]. The relationship between input and the j^{th} component of the output for this type of ANN is given by [47]:

$$d_k(\boldsymbol{\varphi}, \mathbf{W}) = \sigma \left(\sum_{j=1}^M W_{kj}^{(2)} h \left(\sum_{i=1}^D W_{ji}^{(1)} \varphi_i + W_{j0}^{(1)} \right) + W_{k0}^{(2)} \right)$$
(3)

where: $d \in \mathbb{R}^{n_d}$ is the vector whose rows feature damage indices; $\varphi \in \mathbb{R}^{n_s}$ are damage feature vectors; M denotes the number of neurons in the hidden layer; $W_{kj}^{(2)}$ and $W_{k0}^{(2)}$ represent weights and biases of the output layer; and $W_{ji}^{(1)}$ and $W_{j0}^{(1)}$ represent weights and biases of the hidden layer. Activation functions limit a layer's output to a manageable range and need to be nonlinear to guarantee a perceptron's prediction capabilities in a noncompeting ANN [49]. Logistics and hyperbolic tangent functions are two of the most widely used ANN activation functions and are continuously differentiable with a limited range that renders gradient-based optimization feasible [47,49]. Logistic functions limit the range of payer output to 0 and 1, and hyperbolic tangent functions limit the output range to -1 and 1. In this study a hyperbolic tangent sigmoid activation function, $h(\blacksquare)$, is employed for the hidden layer. This function allows for centering layer output around zero. For an extensive discussion of various activation functions readers are referred to [50]. The activation function for the regression output layer $\sigma(\blacksquare)$ is represented by the identity matrix. In a supervised learningbased damage identification scheme, ANN weights W need to be obtained using a set of damage features and corresponding damage indices.

2.3. Overview of POD-ANN for damage identification in the absence of MU

The authors developed a supervised Machine Learning scheme for

detecting, locating, and quantifying the intensity of fatigue-induced damage in railway bridges using POM and ANNs [1]. A neural classifier was trained to categorize response to different load patterns, and a regression ANN was subsequently trained using an ensemble of applied loads to detect possible damage from resulting, categorized POMs. In doing so, the average strain time history root mean square (RMS) for each train passage was used as a feature weight classification and the first snapshot matrix POM was used as the damage feature. Since the damage feature and, subsequently, damage detection accuracy could be sensitive to variations in train load under operational conditions, the ANN needed to be robust to address damage scenarios and train axle loads not used for training.

It is known that Bayesian regularized ANNs are more robust than standard back-propagation ANNs and can decrease the need for cross-validation. Bayesian regularized ANNs are difficult to over-train since evidence procedures provide an objective Bayesian criterion for stopping training using early cessation. Moreover, the regularization term added to their objective function also makes them robust to overfitting. To improve ANN generalization capabilities for damage identification under operational conditions, Bayesian regularization was adopted for optimally finding ANN weights [48,51]. The following objective function needed to be minimized to find the optimal weights:

$$E = \beta E^d + \alpha E^w \tag{4}$$

in which:

$$E^{\mathbf{w}} = \sum_{j=1}^{N_{\mathbf{w}}} \mathbf{w}_j^2 \tag{5}$$

and:

$$E^{d} = \sum_{k=1}^{N} \|\mathbf{t}_{k} - y_{k}(\mathbf{x}_{k}, \mathbf{w})\|^{2}$$
(6)

In Eqs. (4) and (5), \mathbf{w} is a vector that includes all network weights; α and β are objective function parameters; and \mathbf{x}_k and \mathbf{t}_k respectively denote the training input vectors and their corresponding target values for $k=1,2,\cdots,N$. The ratio of objective function parameters determines training emphasis, with larger α/β pushing the network towards generalization and smaller ratios driving the network towards error minimization [52].

For the previous study, the first POM $\varphi \in \mathbb{R}^{n_m}$ of bridge strain response to train passage was used as a damage feature [1,2]. Therefore, when using N_t train passage scenarios and N_d damage scenarios, the following input matrix can be used for training the ANN:

$$[[\boldsymbol{\varphi}^{1,1} \cdots \boldsymbol{\varphi}^{N_d,1}] \cdots [\boldsymbol{\varphi}^{1,N_t} \cdots \boldsymbol{\varphi}^{N_d,N_t}]]_{n_m \times (N_t \times N_d)}$$

$$(7)$$

where superscripts for φ respectively denote the damage and the training scenario.

2.4. Novel damage feature for POD-ANN damage identification in the presence of MU

Based on MU existence and assumptions made on the availability of train axle loads, four possible damage identification scenarios are possible:

- 1. No MU, known loading configurations;
- 2. No MU, unknown loading configurations;
- 3. MU, known loading configurations; and
- 4. MU, unknown loading configurations.

The first two scenarios could be effectively addressed using the framework summarized in Section 2.3 [1,2]. The two latter scenarios feature new MU and POD-based damage features. Proposed methodologies to address these cases are presented in the following two

subsections.

2.4.1. $\triangle POMs$ for training ANNs in the presence of MU, absence of load uncertainty

In general, it is known that structural response POMs are a function of: sensor network topology; sensor types; structure mechanistic and geometric properties; and external loads. These parameters can be represented as:

$$\boldsymbol{\varphi} = \begin{bmatrix} \varphi_1 \\ \vdots \\ \varphi_j \\ \vdots \\ \varphi_n \end{bmatrix} = g(\boldsymbol{\vartheta}^l, \boldsymbol{\vartheta}^g, \boldsymbol{\Xi}, \boldsymbol{\mathcal{F}})$$
(8)

where: $\vartheta^l \in \mathbb{R}^{p_l}$ is the vector that includes p_l parameters that affect local structural response; $\vartheta^g \in \mathbb{R}^{p_g}$ denotes the vector that includes p_g parameters that affect global structural response; $\Xi \in \mathbb{R}^{n_m \times n_d}$ defines coordinates of the sensor network so that φ_j corresponds to $\Xi_{j,1:3}$; and $\mathcal{F} \in \mathbb{R}^m$ denotes the vector of external loads.

If the change in mechanical or geometric properties of a structural member affects the local structural response, any change in POMs would be predominantly local. Assume that different models of a certain structure were available and denoted by \mathcal{M}_i , $i=1,2,\cdots,m$. Also, assume that ϑ^g and Ξ for each \mathcal{M}_i is constant. Finally, it will be assumed that the number of sensors is equal to the number of parameters that govern the local response, i.e. $n_m = p_l$, and that ϑ^l_j affects the structure's response at the sensor installed in $\Xi_{i,1:3}$. As a result:

$$\boldsymbol{\vartheta}^{l} = \begin{bmatrix} \vartheta_{1}^{l} \\ \vdots \\ \vartheta_{j}^{l} \\ \vdots \\ \vartheta_{n}^{l} \end{bmatrix}$$

$$(9)$$

and, for all models \mathcal{M}_i :

$$g(\boldsymbol{\vartheta}^{l} + \Delta_{j}\boldsymbol{\vartheta}^{l}, \boldsymbol{\vartheta}^{g}, \Xi, \boldsymbol{\mathcal{F}}) - g(\boldsymbol{\vartheta}^{l}, \boldsymbol{\vartheta}^{g}, \Xi, \boldsymbol{\mathcal{F}}) \cong \begin{bmatrix} 0 \\ \vdots \\ \Delta \varphi_{j} \\ \vdots \\ 0 \end{bmatrix}$$
(10)

where: $\Delta_j \vartheta^l$ denotes an increment of j^{th} row of the vector ϑ^l . It is shown that the change in the j^{th} component of POM $\Delta \varphi_j$ is proportional to the increment of j^{th} row of the vector ϑ^l :

$$\Delta \varphi_j \propto \Delta_j \vartheta^l. \tag{11}$$

It follows that, if $\Delta \varphi$ is used as a damage feature within a POD-ANN damage identification framework, and ϑ^g , Ξ and $\mathcal F$ are constant, any of $\mathscr M_i$ models could effectively generate damage scenarios required for training the ANNs. Extensive numerical investigations in Section 4 support this premise and show that, while φ globally varies by $\Delta_j \vartheta^l$ for any $\mathscr M_i$ subjected to the same external load, $\Delta \varphi$ varies locally. When the damage scenario is a local phenomenon, it will produce an increment in the value of the parameter that changes local structural response:

$$\Delta \varphi = \varphi^d - \varphi^h \tag{12}$$

where: φ^d denotes the first POM of the structure in a damaged state; and φ^h stands for the first POM of the healthy, baseline structure. To train the ANN for damage detection, the following features for N_d damage scenarios are proposed:

$$\left[\Delta \boldsymbol{\varphi}^1 \quad \cdots \quad \Delta \boldsymbol{\varphi}^{N_d}\right]_{n_m \times N_d} \tag{13}$$

where the superscript for $\Delta \varphi$ indicates the damage scenario.

If a suitable model class is constructed for the actual structure and MUs are predominantly stemming from unknown parameter values rather than mechanical characterization, one can argue that $\Delta POMs$ obtained from response measured before and after a deficiency happens could be reasonably approximated by $\Delta POMs$ from models \mathcal{M}_i :

$$\Delta \varphi_{exp} \cong \Delta \varphi_{\mathscr{M}_i} \tag{14}$$

It might be challenging to calculating $\Delta \varphi$ for real-world scenarios due to difficulty associated with having the same loading configurations for healthy and damaged conditions. However, this scenario was included to account for situations where owners would be willing to run the same train for assessing bridge health. For example, owners might be able to run a train composed of 3 or 4 locomotives with a consistent speed periodically to improve health assessment capabilities. This scenario could also be used for roadway bridges where testing vehicle loads, speeds and locations are known and controlled.

2.4.2. Approximating POMs for training ANNs in the presence of MU and load uncertainty: Hybrid experimental-numerical approach

The premise from Section 2.4.1 is used herein for approximating damage scenario POMs. Using POMs of a healthy structure obtained from experimental data and Δ POMs of damage scenarios obtained from the numerical model \mathcal{M}_i one can deduce the following when considering Eqs. (12) and (14).:

$$\varphi^d \cong \widehat{\varphi}^d = \varphi^h_{exp} + \Delta \varphi_{\mathscr{M}_i} \tag{15}$$

where $\hat{\varphi}$ denotes an estimate of φ . Estimated POMs then could be used as input for training the ANN:

$$[[\widehat{\varphi}^{1,1} \cdots \widehat{\varphi}^{N_d,1}] \cdots [\widehat{\varphi}^{1,N_t} \cdots \widehat{\varphi}^{N_d,N_t}]]_{n_m \times (N_t \times N_d)}$$

$$(16)$$

Extensive numerical analyses in Section 4 again support this premise.

3. Studied bridge, instrumentation, numerical model

The structure under study is an in-service, multi-span, railway bridge located in central Nebraska. The bridge is comprised of rolled and riveted, built-up, steel elements. Bridge spans include simply-supported through-girder and truss systems. This study focuses on a truss span with span geometry, field testing instrumentation and its numerical model being described in the following sections. Additional details are provided in a previous publication [5].

3.1. Studied span

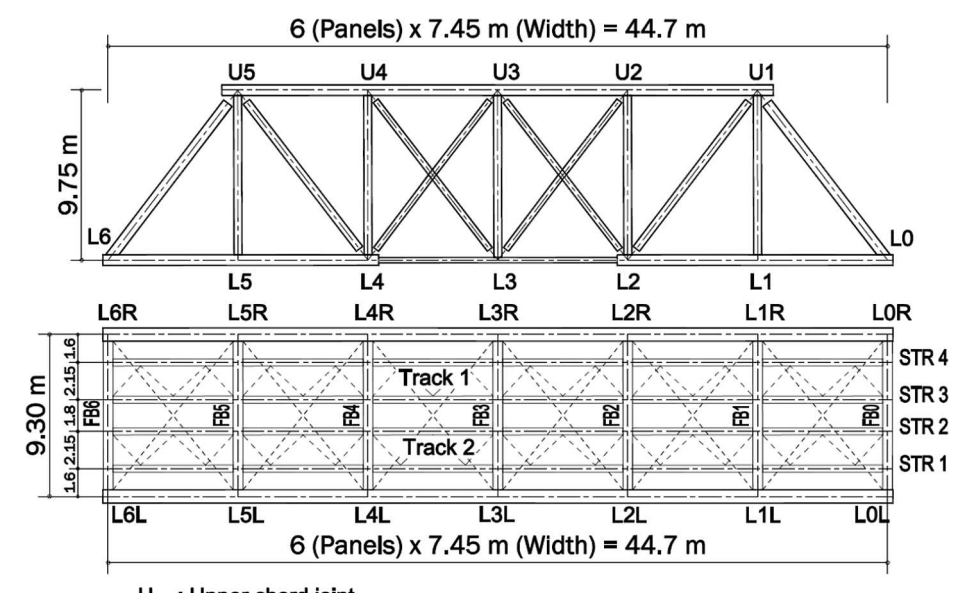
The studied truss span is 44.7 m long and contains six panels with stringers connected to floor beams that are spaced at 7.45 m on-center longitudinally. The stringers are laterally spaced at 2.15 m on-center and support two tracks spaced laterally 3.95 m center-to-center. A lateral wind bracing system is provided with laterals being provided. Truss diagonals, end-posts, verticals, top chords and end bottom chords are riveted built-up members while midspan diagonals and bottom chords are eyebars of varying thickness. Floor beams and stringers are riveted, built-up I-sections with the floor beams composed of a web plate, flange angles and cover plates while the stringers have a web plate and angles only. Lower lateral bracing members are single angles of varying dimensions while upper lateral bracing are laced angles. Stringer lateral bracing is also provided using single angles located close to the top flange. Elevation and plan views of the studied span are found in Fig. 1.

3.2. Instrumentation plan

The implemented SHM system utilized strain time-histories to measure truss response to train loads. Strain measurements were selected since they are direct indicators of local damage, such as that stemming from fatigue. These measurements also maximize data significance while minimizing sensor numbers. A sensitivity analysis was carried out to ensure proposed instrumentation provided enough information for the identification of stringer-to-floor beam connection damage [5]. It was determined that 20 strain transducers installed at stringer bottom flanges close to stringer-to-floor beam connections would yield precise damage identification results. Strains were extracted from numerical investigations or measured from field tests at these locations. A plan view showing instrument locations is shown in Fig. 2.

4. Numerical validation

The objective of the numerical investigation was to identify a robust damage feature that is independent of MU and could be used to identify damage scenarios from field measured strains. Five numerical models



U : Upper chord joint
L : Lower chord joint
FB : Floor beam
STR : Stringer

Fig. 1. Truss elevation and plan view.

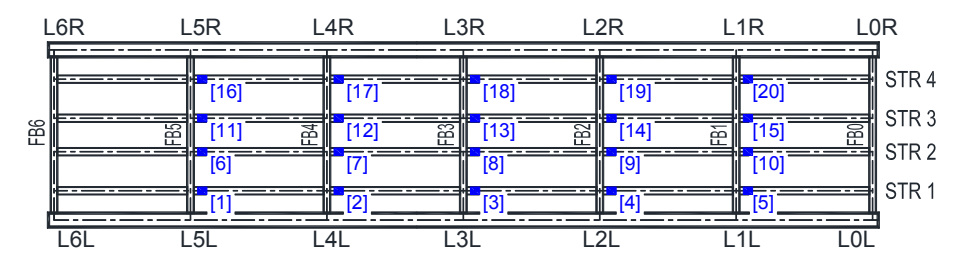


Fig. 2. Truss span instrument and damage locations (IL and DL).

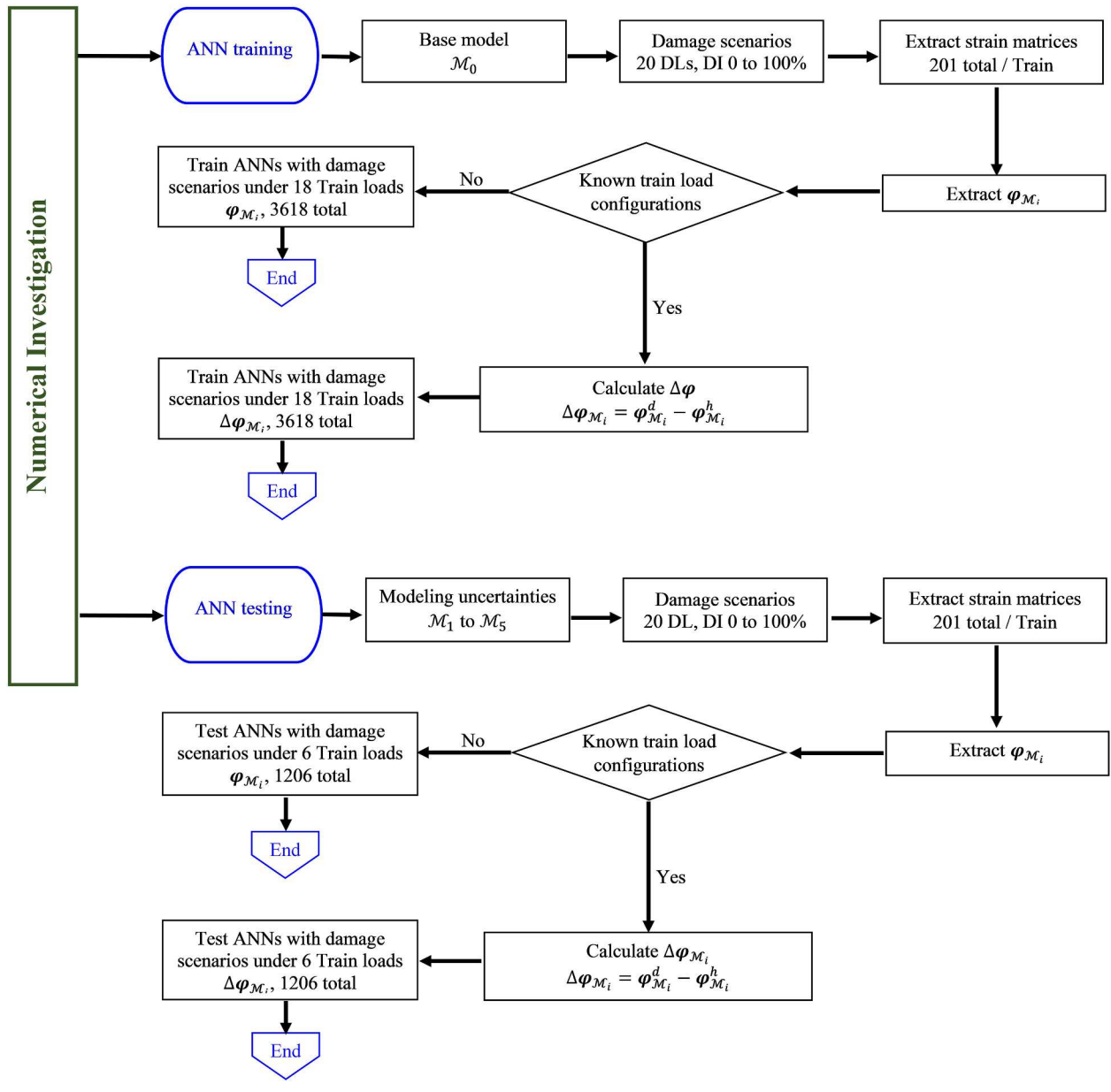


Fig. 3. Numerical investigation flowchart.

helped identify the feature, with one being the base model with no MU and the rest including simulated MUs. The most consistently recognized damage feature was selected and applied to data produced from the numerical models and field tests. A flowchart describing the numerical validation procedure is shown in Fig. 3.

4.1. Numerical model

The FE model was developed using SAP2000 and validated against measured data from the field tests. The model contained the trusses, stringers, floor beams and bracing systems. Riveted truss elements and floor beams were modeled as rigidly connected at both ends while truss eyebars and bracing members were modeled as pinned at their ends. Stringers connections were modeled using rotational springs to

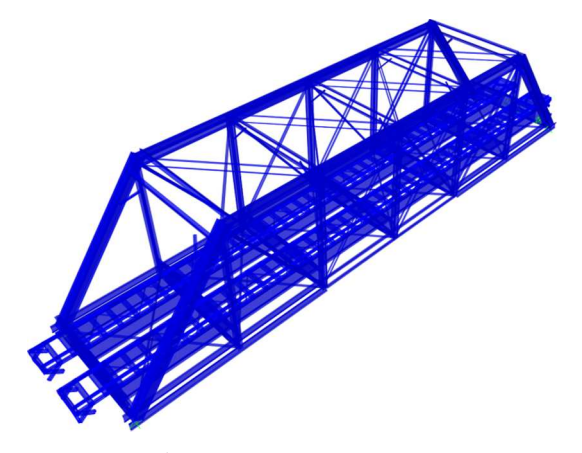


Fig. 4. SAP2000 isometric view.

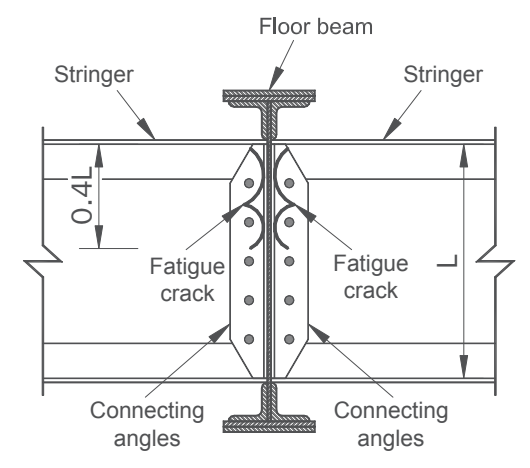


Fig. 5. Depiction of fatigue cracks in stringer-to-floor beam connecting angles [7].

facilitate simulating stringer-to-floor beam connection damage as a reduction in rotational stiffness. In earlier research work, model calibration was completed so that measured strain time histories and their corresponding values from the three-dimensional finite element model had good agreement [5]. Parameters used to improve model accuracy included explicitly modeling the rails, incorporating vertical offsets for floor system members to better account for structural element locations,

Table 1 MU cases.

Model	Assignment	Normalized rotational spring coefficient (M_i/M_0)
\mathcal{M}_0	Uniform	1.00
\mathcal{M}_1	Uniform, increase $+80\%$ of \mathcal{M}_0	1.80
\mathcal{M}_2	Uniform, decrease -50% of \mathcal{M}_0	0.50
M_3	Random, ± 25% of Mo	Between 0.76 and 1.25
\mathcal{M}_4	Random, \pm 50% of \mathcal{M}_0	Between 0.53 and 1.45
\mathcal{M}_5	Random, \pm 100% of \mathcal{M}_0	Between 0.23 and 1.92

modifying bottom lateral axial stiffness and varying stringer end connections bending and axial stiffness. The final calibrated model included the rails, vertical offsets and modified stringer end connection bending fixity ratios. For more details about the calibration activities, see [5]. This calibrated model is used herein as one of the MU cases and is denoted as \mathcal{M}_1 . An isometric view of the developed model is shown in Fig. 4 [5].

Published fatigue laboratory tests of two panels having stringers with riveted end connections showed a gradual decrease in rotational stiffness associated with the crack growth [7]. As a result, a semi-rigid connection would ultimately become a pinned connection. It was reported that the developed crack vertical projection depth at which pinned behavior was observed was when the crack propagated to approximately 40% of the angle leg length. Fig. 5 depicts typically developed fatigue cracks in the angle legs and Fig. 6 shows the corresponding decreases in rotational stiffness [7]. Continuously reducing connection rotational stiffness could be used to simulate crack propagation and the associated reduction in stringer end strains. For the current study, the damage was simulated at the 20 stringer ends by reducing end spring rotational stiffness 0% to 100% reduction (i.e., DI = 0% to DI = 100%) in increments of 10%. Stiffness reductions were applied to one stringer end at a time, with other connections being undamaged and, as stated earlier, Damage Locations (DLs) corresponded to instrument locations in Fig. 2.

The bridge models were excited using real train loads. Weigh-In-Motion (WIM) recorded loading configurations for 81 trains of varying axle loads, axle spacing's and overall lengths that traversed the bridge were selected. The numerical analyses and extraction of significant results for each of the studied damage scenarios were automatically performed using MATLAB [53] and SAP2000 Open Application

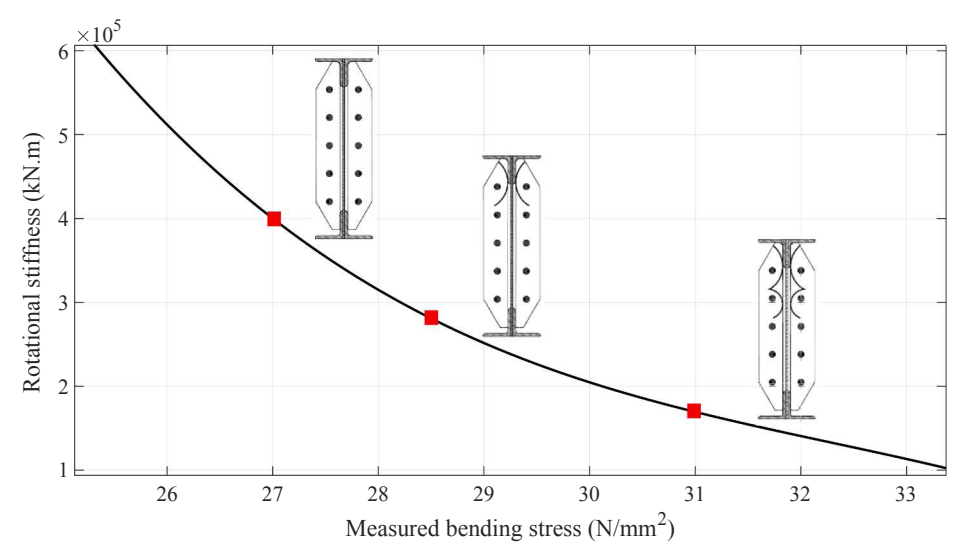


Fig. 6. Rotational stiffness reductions associated with crack propagation [7].

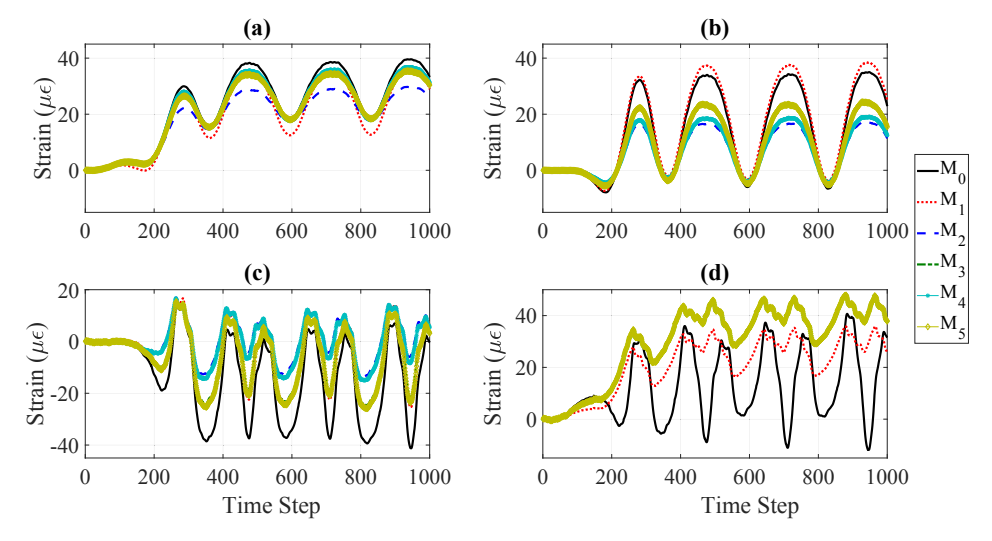


Fig. 7. Strain time-history comparisons for different MU scenarios: (a) DI 40% at DL 3; (b) DI 60% at DL 8; (c) DI 80% at DL 13; and (d) DI 100% at DL 18.

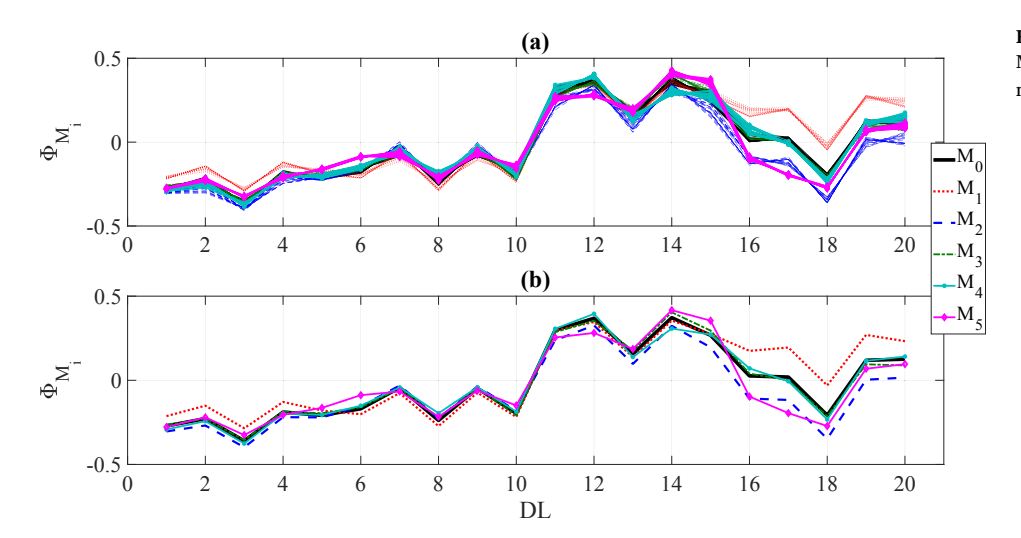


Fig. 8. Healthy POM variations associated with MU scenarios $(\varphi^h_{\mathcal{M}_l})$: (a) $\varphi^h_{\mathcal{M}_l}$; and (b) $\varphi^h_{\mathcal{M}_l}$ mean

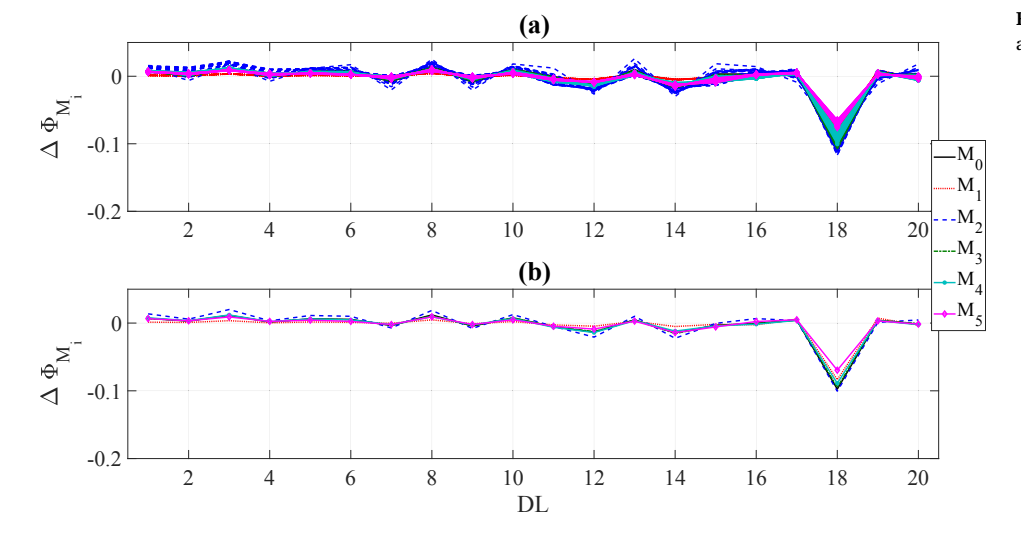


Fig. 9. $\Delta \varphi_{\mathcal{M}_i}$ at DL 18 with DI 80%: (a) $\Delta \varphi_{\mathcal{M}_i}$; and (b) $\Delta \varphi_{\mathcal{M}_i}$ mean.

Programming Interface (OAPI) for the 81 trains [1]. Extracted strains at the instrumented locations were placed into matrices with each matrix containing time histories for one train passage "snapshot." RMS means of the snapshot matrices were used to sort train events and trains were divided into four different groups based on resulting ranges. It is

important to note that a strong correlation was observed between strain snapshot RMS and train loads, with higher RMS shown to represent heavily loaded trains [1]. The effect of train speed was also investigated, and it was observed that variation in speed could influence POD-ANN framework results. To reduce speed effects on POD-ANN

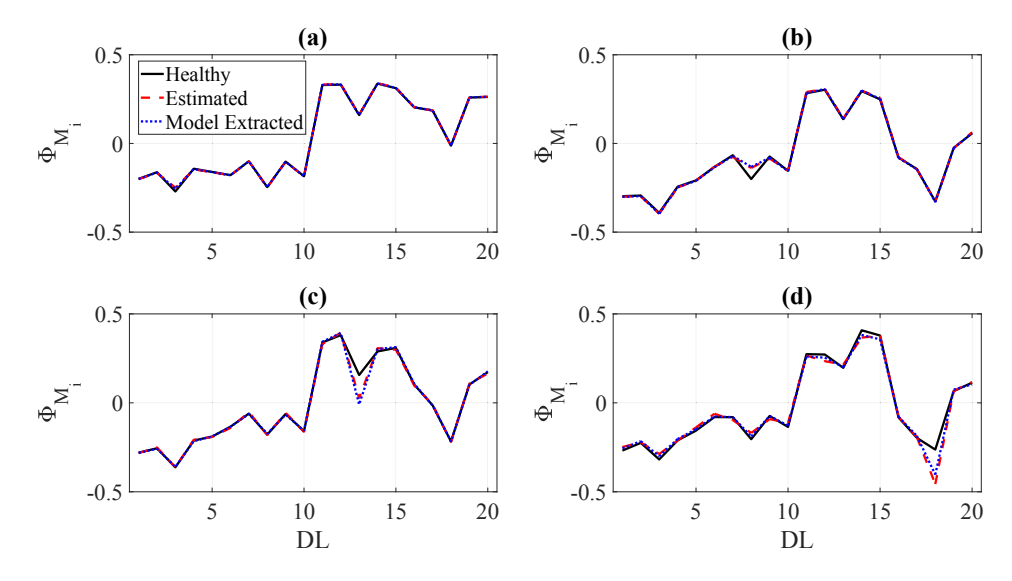


Fig. 10. $\widehat{\varphi}_{\mathcal{M}_i}^d$ accuracy comparisons: (a) DI 40% at DL 3 with \mathcal{M}_1 ; (b) DI 60% at DL 8 with \mathcal{M}_2 ; (c) DI 80% at DL 13 with \mathcal{M}_4 ; and (d) DI 100% at DL 18 with \mathcal{M}_5 .

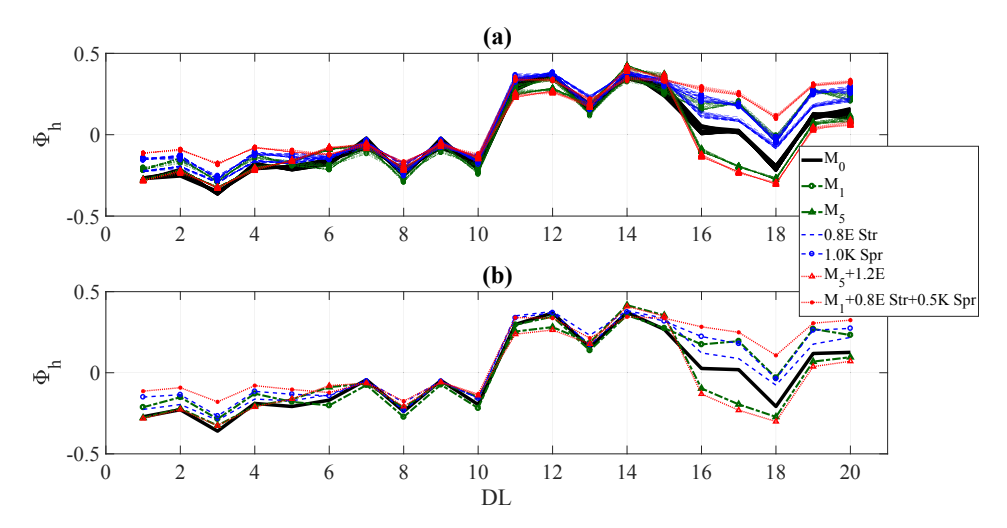


Fig. 11. Healthy POM variations for additional MU $(\varphi_{\mathcal{M}_i}^h)$ cases: (a) $\varphi_{\mathcal{M}_i}^h$; and (b) $\varphi_{\mathcal{M}_i}^h$ mean.

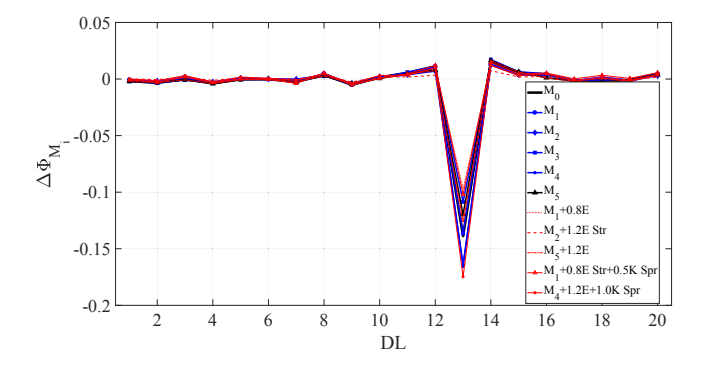


Fig. 12. $\Delta \varphi_{\mathcal{M}_i}$ at DL 13 with DI 80% for multiple MU sources.

framework damage detection, it was concluded that selected snapshots should include the same number of strain peaks (i.e., having the same number of strain peaks under trains of varying speed would produce different snapshot sizes). A subset of the 81 trains, ones with RMS causing higher strains and POMs of minimal variation, were selected. This resulted in 24 trains being used for the current study [1].

The numerical study completed herein considered strain POM variations caused by: (i) non-stationary (i.e., moving) train loads; (ii) DLs and DIs; and (iii) MUs. Analyses for various trains loadings and DL/DI combinations were completed automatically using MATLAB and

SAP2000 OAPI. For each simulated MU, the number of associated analyses was 4824 damage scenarios, which corresponded to 24 trains, 10 DIs and 20 DLs.

The authors were unable to find resources that helped couple MATLAB code to the SAP2000 OAPI to complete automated analyses and output extraction. As a result, online resources for the processes developed for the current study are provided. Online Resource 1 contains MATLAB code for running multi-step analyses and Online Resource 2 details relationships between MATLAB coding and SAP2000 OAPI windows for some of the crucial functions.

4.2. MU cases

Stringer-to-floor beam end-fixity ratios vary widely and, as a result, no clearly defined relationship exists. Design practice assumes that these connections would transfer shear force only; however, laboratory and field tests indicated a high amount of end fixity [4,7–10,12]. Stringer-to-floor beam connection end fixity ratio was shown to influence stress time histories significantly. As a result, fatigue crack development was mainly attributed to out-of-plane deformation of connecting angles and stress concentrations at rivets heads [10].

Because of significant variations of end fixity ratios observed from the tests, higher discrepancies between actual and modeled ratios are expected. As a result, end fixity ratio was selected as the major MU factor for the current study. As stated earlier, the base model had no MU

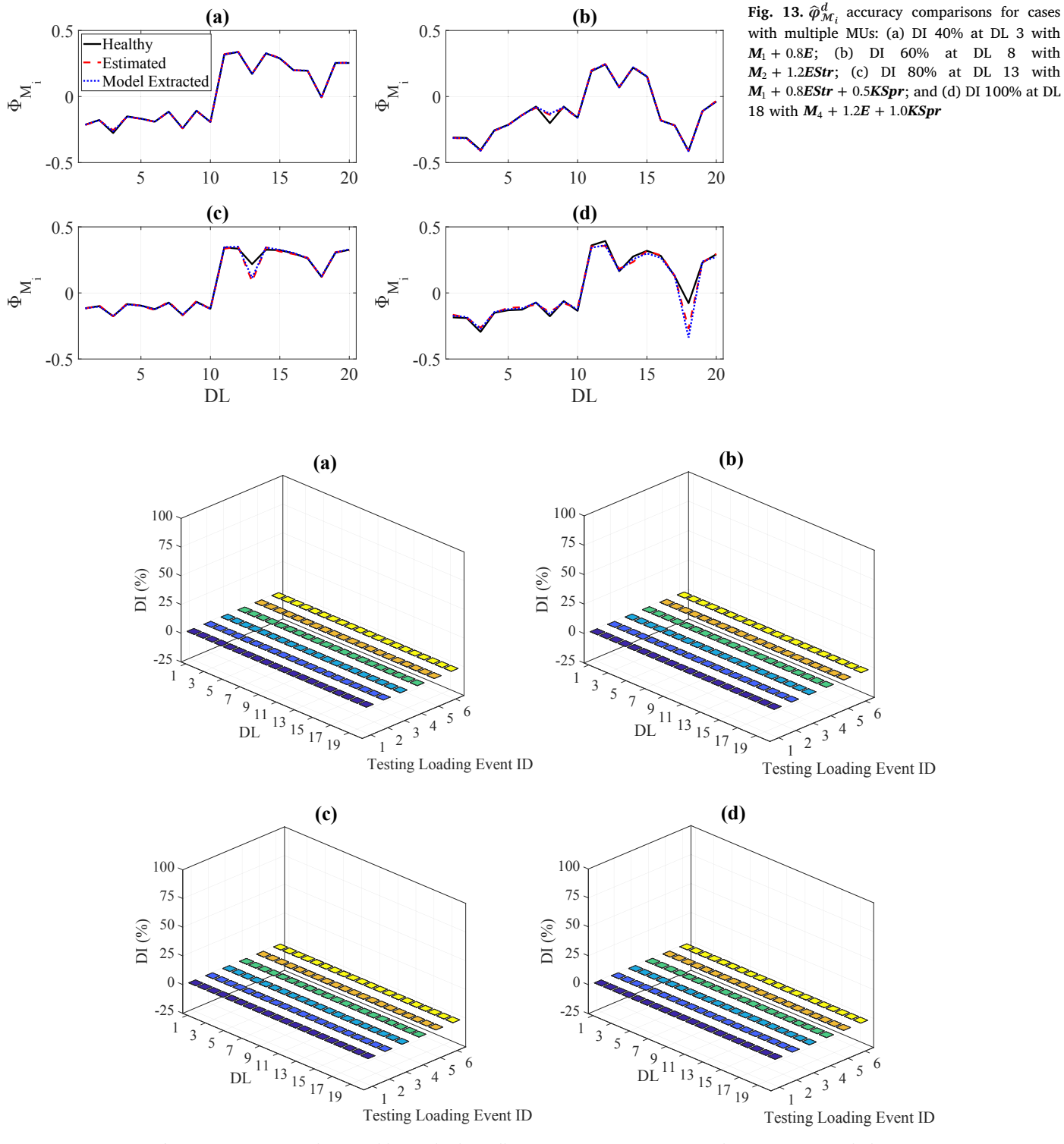


Fig. 14. ANN testing with MU and known loading, all testing events, DI 0%: (a) \mathcal{M}_1 ; (b) \mathcal{M}_2 ; (c) \mathcal{M}_4 ; and (d) \mathcal{M}_5 .

(\mathcal{M}_0) and the end fixity ratio was assumed to be 67% of that for a fully continuous stringer [7]. This corresponded to a linear rotational spring coefficient of 803,435 kN-m/rad applied uniformly to all stringer ends. The first 2 MU cases (\mathcal{M}_1 and \mathcal{M}_2) uniformly varied all stringer end fixity ratios by +80% and -50% of that assigned in \mathcal{M}_0 , which corresponded to assigned spring coefficients of 1,446,183 and 401,717 kN-m/rad for \mathcal{M}_1 and \mathcal{M}_2 , respectively. The 80% increase was based on results from model validation activities [5]. The other 3 MU cases (\mathcal{M}_3 to \mathcal{M}_5) used randomly modified end fixity ratios at \pm 25, 50, and 100% of the \mathcal{M}_0 case, which produced randomly varying coefficients at each

connection. Assigned spring coefficients are listed in Table 1 for each stringer.

To demonstrate the influence of selected MU cases on strain response, results were compared for \mathcal{M}_0 to \mathcal{M}_5 cases where significant change in strain time-histories was observed, especially for Instrumented Locations (IL) located beneath the unloaded track (i.e., DL 11 to DL 20). A comparison of strains is shown in Fig. 7 for selected MU cases having 40, 60, 80 and 100% DI at DLs 3, 8, 13 and 18. Clearly apparent changes in strain from \mathcal{M}_0 were observed for \mathcal{M}_1 to \mathcal{M}_5 strain time-histories.

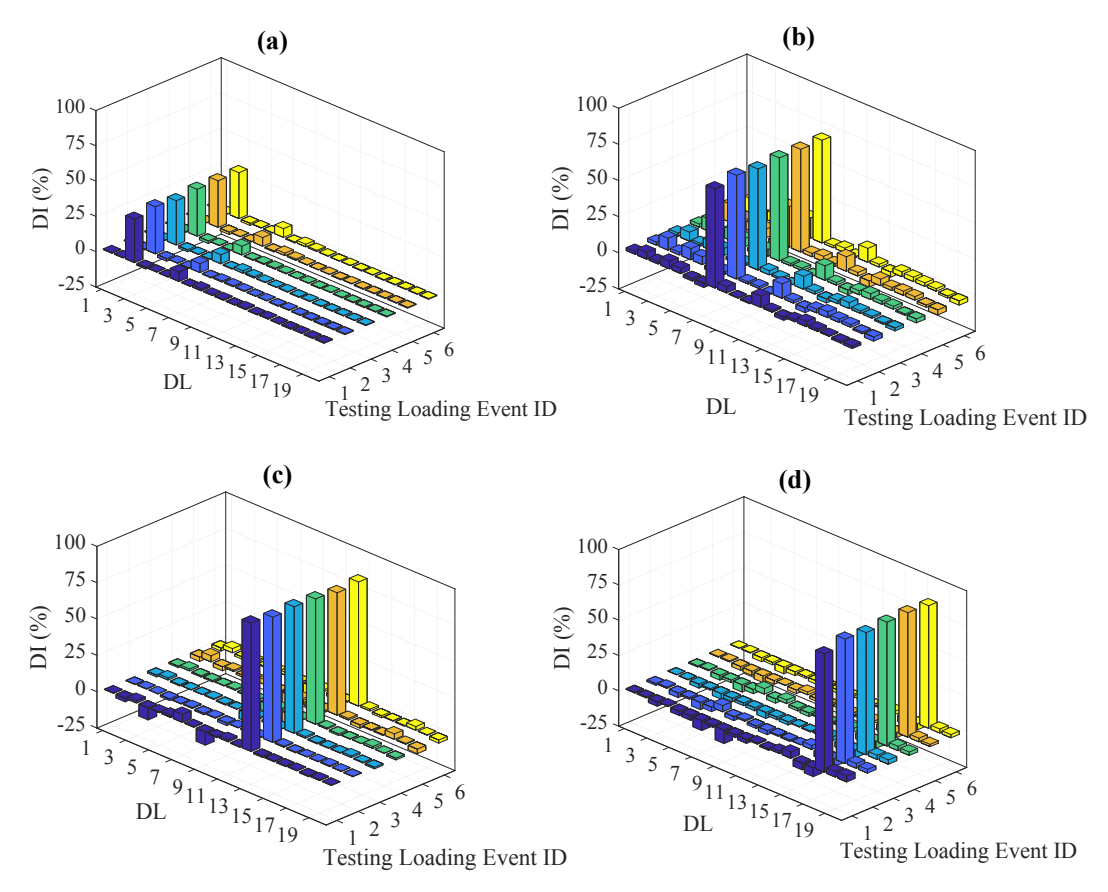


Fig. 15. ANN testing with MU and known loading, all testing events: (a) DI 40% at DL 3, \mathcal{M}_1 ; (b) DI 60% at DL 8, \mathcal{M}_2 ; (c) DI 80% at DL 13, \mathcal{M}_4 ; and (d) DI 100% at DL 18, \mathcal{M}_5 .

Table 2
MU and known load testing results.

Figure	Subplot	MU case	Simulated DI and DL	Detected DI at simulated DL	False positive and negative DIs
Fig. 15	a	\mathcal{M}_1	40% at DL 3	31–33%	3%
	b	\mathcal{M}_2	60% at DL 8	66-67%	15 and 25%
	c	\mathcal{M}_4	80% at DL 13	86-88%	9 and 9%
	d	M_5	100% at DL 18	91-95%	4 and 10%
Fig. 16	a	\mathcal{M}_1	70% at DL 15	60-61%	4% and 8%
	b	\mathcal{M}_2	70% at DL 15	73-76%	10% and 12%
	c	\mathcal{M}_4	70% at DL 15	67-71%	51% and 18%
	d	Ms	70% at DL 15	62-65%	10% and 18%

4.3. Robustness of ΔPOMs to MUs

Strains were extracted at the ends highlighted in Fig. 2 and corresponding $\varphi_{\mathcal{M}_i}$ were calculated for each of the considered \mathcal{M}_i cases and damage scenarios. Fig. 8a shows a comparison of $\varphi_{\mathcal{M}_i}^h$ for the 24 train events for the \mathcal{M}_i cases where significant change was observed due to MUs and minimal effects observed from load variations. Fig. 8b depicts the mean for $\varphi_{\mathcal{M}_i}^h$ for considered \mathcal{M}_i cases, which again highlights significant $\varphi_{\mathcal{M}_i}^h$ changes associated with MUs. Since $\varphi_{\mathcal{M}_i}^h$ varies significantly for the MUs, it cannot be classified as a robust damage feature that could eliminate or reduce MU effects. To eliminate $\varphi_{\mathcal{M}_i}$ variations attributed to examined MUs, $\Delta\varphi_{\mathcal{M}_i}$ was calculated for each damage scenario as:

$$\Delta \varphi_{\mathcal{M}_i} = \varphi_{\mathcal{M}_i}^d - \varphi_{\mathcal{M}_i}^h \tag{17}$$

Resulting $\Delta \varphi_{\mathscr{M}}$ showed that variations due to MUs were significantly reduced when compared against $\varphi_{\mathscr{M}}$ variations. As shown in

Fig. 8, DL 18 experienced the highest variation in $\varphi_{\mathcal{M}_i}^h$; however, when $\Delta \varphi_{\mathcal{M}_i}$ was used the variation was significantly lower and the DL accurately identified. Fig. 9a shows that $\Delta \varphi_{\mathcal{M}_i}$ at DL 18 for DI 80% and the considered train events showed minor variation observed for examined MUs and train loadings. Fig. 9b compares the mean of $\Delta \varphi_{\mathcal{M}_i}$ for the MUs and again shows minor variations. These minor variations indicate that, for the studied bridge, model and scenarios, $\Delta \varphi_{\mathcal{M}_i}$ could be considered a robust damage feature that is largely independent of MUs and train loads

Since generating damage scenarios for an in-situ bridge is largely impossible, an alternate way to develop damage scenarios is by implementing $\Delta \varphi_{\mathscr{M}_i}$ as a damage feature. To do so, $\hat{\varphi}^d$ was calculated to generate damage scenarios as a function of $\varphi^h_{\mathscr{M}_i}$ to $\varphi^h_{\mathscr{M}_i}$ and $\Delta \varphi_{\mathscr{M}_0}$ as:

$$\hat{\boldsymbol{\varphi}}_{\mathcal{M}_{i}}^{d} = \Delta \boldsymbol{\varphi}_{\mathcal{M}_{0}} + \boldsymbol{\varphi}_{\mathcal{M}_{i}}^{h} \tag{18}$$

Since $\Delta \varphi_{\mathscr{M}_i}$ variations due to MUs were observed to be minor, $\widehat{\varphi}^d_{\mathscr{M}_i}$ (i.e., estimated) is expected to match closely $\varphi^d_{\mathscr{M}_i}$ (i.e., the model extracted). To ensure the applicability of $\widehat{\varphi}^d_{\mathscr{M}_i}$ for simulating actual damage scenarios, comparisons between $\varphi^h_{\mathscr{M}_i}$, $\widehat{\varphi}^d_{\mathscr{M}_i}$ and $\varphi^d_{\mathscr{M}_i}$ where completed and close agreement was observed between $\widehat{\varphi}^d_{\mathscr{M}_i}$ and $\varphi^d_{\mathscr{M}_i}$ at different MUs. One example of those comparisons shown in Fig. 10 for DIs of 40, 60, 80 and 100% simulated at DL 3, 8, 13 and 18 for \mathscr{M}_1 to \mathscr{M}_5 . The comparison showed a very close match between $\widehat{\varphi}^d_{\mathscr{M}_i}$ (i.e., estimated from $\Delta \varphi_{\mathscr{M}_0}$ and $\varphi^h_{\mathscr{M}_i}$) and $\varphi^d_{\mathscr{M}_i}$ (i.e., calculated from deficient models strains \mathscr{M}_1 to \mathscr{M}_5) for various DIs, DLs and MUs. The results proved that generating damage scenario POMs ($\widehat{\varphi}^d_{\mathscr{M}_i}$) from $\Delta \varphi_{\mathscr{M}_0}$ of one model and $\varphi^h_{\mathscr{M}_i}$ of another model is possible. As a result, a similar approach could be applied to generate $\widehat{\varphi}^d_{exp}$ from φ^h_{exp} from measured strains. In other words, $\widehat{\varphi}^d_{exp}$ can be generated from $\Delta \varphi_{\mathscr{M}_i}$ and φ^h_{exp} .

It is important to note that, while inaccurately modeling stringer to

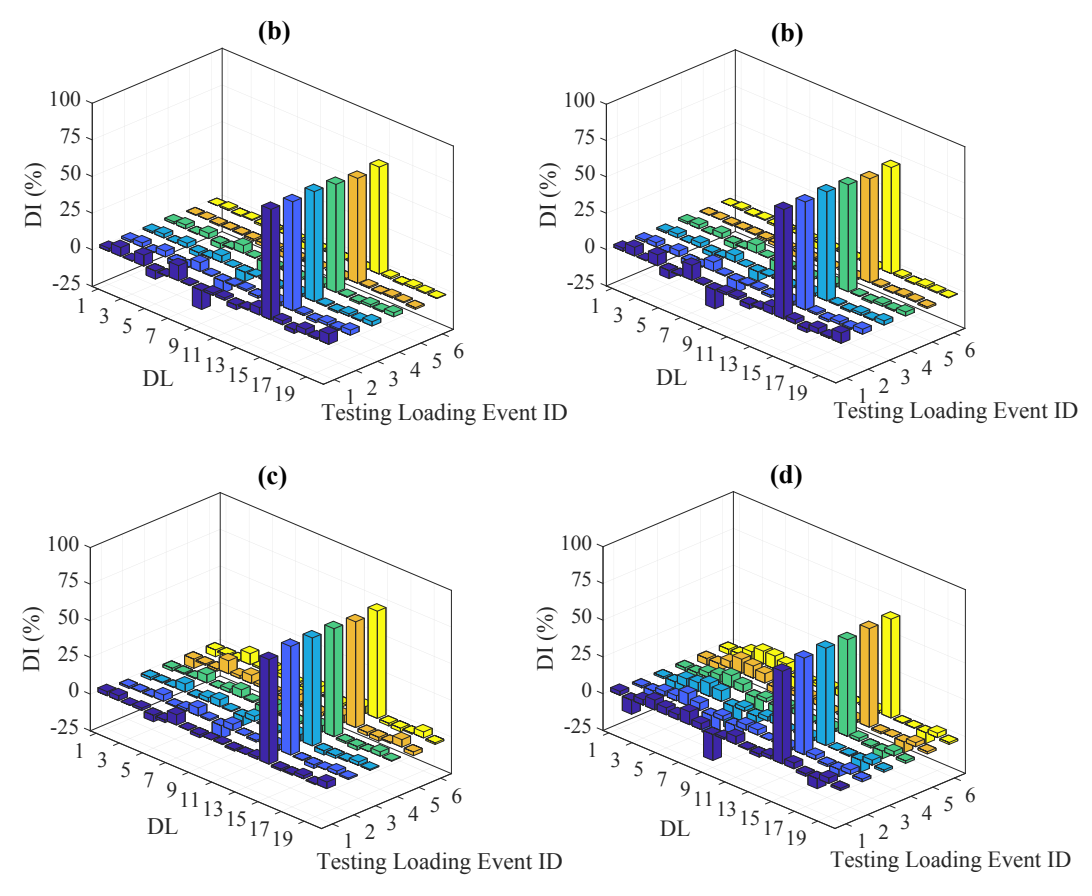


Fig. 16. ANN testing with MU and known loading, DI 70% at DL 15, all testing events: (a) \mathcal{M}_1 ; (b) \mathcal{M}_2 ; (c) \mathcal{M}_4 ; and (d) \mathcal{M}_5 .

floor beam connections is not the only source of MU, a significant influence on predicted response accuracy is anticipated to occur when the connections are inaccurately represented. Another potential source of MU could include inaccurate representation of (1) material properties, represented using inaccurate elastic moduli (E), and (2) bridge support conditions. To examine the influence of these MU sources on φ , additional cases were studied. These included: (i) uniformly increasing or reducing E of the entire bridge by 20% (1.2E and 0.8E); (ii) uniformly or reducing E of the stringers (1.2E Str and 0.8E Str); and (iii) using longitudinal springs at the free (roller supported) end to account for frozen bearings, with spring coefficients set to 50 and 100% of the bridge longitudinal stiffness (K) (0.5 KSpr and 1.0 KSpr). The longitudinal bridge stiffness was estimated as the inverse of the longitudinal displacement at the roller ends of the bridge under longitudinal point loads. In addition, the effects of multiple MU sources on φ were also examined as follows: (i) $M_1 + 0.8E$; (ii) $M_2 + 1.2EStr$; (iii) $M_5 + 1.2E$; (iv) $M_1 + 0.8EStr + 0.5KSpr$; and (v) $M_4 + 1.2E + 1.0KSpr.$

Fig. 11 contains representative comparisons between $\varphi_{\mathcal{M}_0}$ and φ for M_1 and M_5 and the sources of MU outlined in the preceding paragraph. As can be seen in the figure, including additional MU sources or their combinations slightly influenced φ when compared against the M_1 to M_5 cases, with agreement improving when a validated version of the base model was used. Fig. 12 shows additional comparisons between $\Delta \varphi_{\mathcal{M}_1}$ at DL 13 for DI 80%. Minor variations between the M_1 to M_5 cases and the additional cases were again observed. These findings support using MU cases M_1 to M_5 for the current study and also support the premise that $\Delta \varphi_{\mathcal{M}_1}$ is a robust damage feature largely independent of MUs.

Comparisons between $\varphi^h_{\mathcal{M}_i}$, $\widehat{\varphi}^d_{\mathcal{M}_i}$ and $\varphi^d_{\mathcal{M}_i}$ for multiple MUs were also completed with excellent agreement observed. An example of those comparisons is shown in Fig. 13 for DIs of 40, 60, 80 and 100% at DL 3, 8, 13 and 18. The results prove that generating damage scenario POMs

 $(\widehat{\boldsymbol{\varphi}}_{\mathcal{M}_i}^d)$ from $\Delta \boldsymbol{\varphi}_{\mathcal{M}_i}$ of one model and $\boldsymbol{\varphi}_{\mathcal{M}_i}^h$ from another model is possible when multiple MUs are included.

4.4. ANN training and testing data sets

Training data was generated for the 10 DIs at each DL shown in Fig. 2. A total of 4800 damage scenarios corresponding to each MU were developed by sequentially varying DIs at the designated DLs for the 24 train events. ANNs were trained using MATLABs *Neural Net Fitting* toolbox, which produced a nonlinear regression that, in turn, helped establish damage detection effectiveness.

Extracted $\varphi^h_{\mathcal{M}_i}$ and $\varphi^d_{\mathcal{M}_i}$ values were used to train and test the ANNs. Of the 24 trains, 18 were used to train the ANNs and six to test their ability to detect DLs and DIs. More details about the process can be found elsewhere [1]. The four training scenarios discussed in Section 2.4 were considered.

For a given MU and known loading scenario, $\Delta \varphi_{\mathscr{M}_0}$ was used to train the ANNs and $\Delta \varphi_{\mathscr{M}_1}$ to $\Delta \varphi_{\mathscr{M}_2}$ used to test them. The training and testing data sets differed based on: (i) the presence of or absence of MUs; and (ii) training load events differing from those used for testing. For a realworld application, however, train loading configurations should be known to calculate $\Delta \varphi$ (i.e., it is calculated as the difference between two φ for the same train event). For each MU and unknown loading scenario, $\widehat{\varphi}_{\mathscr{M}_1}^d$ was then adopted to impose damage. Testing was completed for $\varphi_{\mathscr{M}_1}^d$, which was directly calculated from deficient numerical models. These training and testing data sets differed because: (i) $\widehat{\varphi}_{\mathscr{M}_1}^d$ involved MUs used to train ANNs while $\varphi_{\mathscr{M}_1}^d$ was used to test them; and (ii) training train events loadings were different from testing loads.

A desktop computer having a multi-core architecture and a Windows 7 64-bit operating system was used to perform ANN training. The computer's Central Processing Unit was an Intel Xeon E5-2630 2.4 GHz processor with 8 Cores, 32 GB DDR4 of RAM and a 20 MB

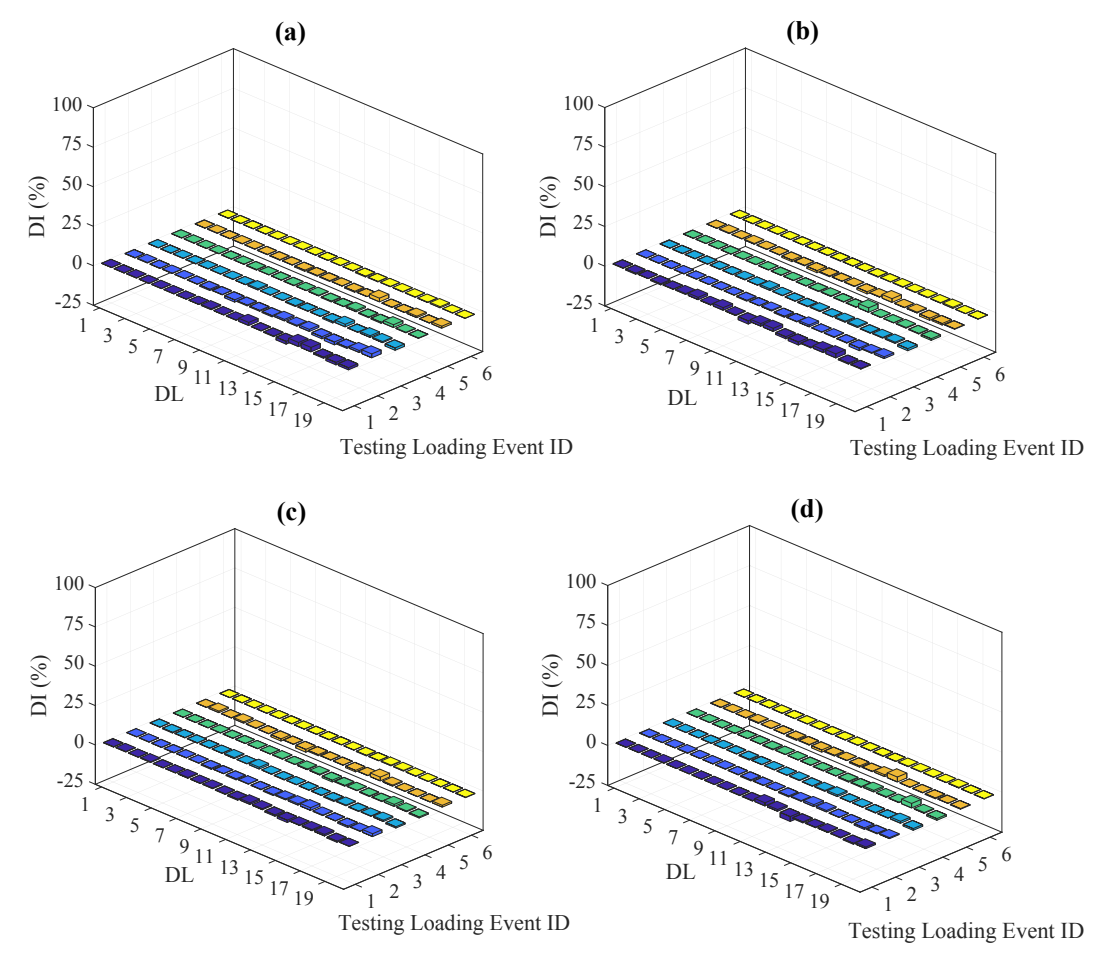


Fig. 17. ANN testing with MU and unknown loading, all testing events, DI 0%: (a) M₁; (b) M₂; (c) M₄; and (d) M₅

Smart Cash. Training time was between 1050 and 1300 min for each considered MU case.

4.5. Damage identification results

In this section, POD-ANN framework testing results are presented and discussed. Testing was completed using a total of six train "Loading" events that were not included in the ANN training process, as mentioned earlier.

4.5.1. Training with MU and known loads

One of the most critical issues with any health monitoring system is avoiding false alarms, which are an erroneous report of damage detection. To ensure the developed method was robust against false alarms, POMs for healthy scenarios subjected to testing train "loading events" were used to test trained ANNs for a given MU. Fig. 14 shows testing results when trained using MUs and known loads for healthy scenarios. It plots ANN testing for healthy scenarios under selected testing loading events for \mathcal{M}_1 , \mathcal{M}_2 , \mathcal{M}_4 and \mathcal{M}_5 where the likelihood of false alarms is assumed to be low. It was observed that, for events associated with the six trains selected for ANN testing, the maximum false-positive DI was approximately less than 0.1%, which was deemed to be low when compared against the actual DI of 0%. These results support the premise that the method would successfully detect damage with the need for determining an acceptable threshold via long-term monitoring.

To further evaluate the ability of the proposed methodology to detect DL and DI for various MUs, ANN damage detection effectiveness at instrumented locations was studied. Results of some of the damage

scenarios are described herein for the sake of brevity. DLs and DIs were arbitrary with DLs of 3, 8, 13 and 18 chosen and DIs of 40, 60, 80 and 100% used for \mathcal{M}_1 , \mathcal{M}_2 , \mathcal{M}_4 and \mathcal{M}_5 . Results from ANNs for all train events are shown in Fig. 15. DIs and DLs were detected with reasonable accuracy for the considered MU cases. However, false positives and negatives were observed with varying magnitudes depending on the levels of MU and DL. Results presented in Fig. 15 are summarized in Table 2.

To illustrate the effect of MU level on DL and DI detection, another comparison between MUs at DL 15 and a DI of 70% under all testing loading events was completed as shown in Fig. 16. As demonstrated in the figure, the accuracy of detecting DL and DI varies based on MU level with both false-positives and negatives being observed. A summary of the testing results are also shown in Fig. 16 are listed in Table 2.

4.5.2. Training with MU and unknown loads

Fig. 17 shows testing results for MUs, unknown loads and healthy scenarios. It was observed that, for events associated with the six trains selected for ANN testing, the maximum false-positive DI was approximately less than 3%, which was considered low given the actual DI of 0%. As discussed previously, these results supported that the method would successfully detect damage with the need for determining an acceptable threshold via long-term monitoring since similar observations were made in the previous testing results.

Fig. 18 shows another example of ANN testing for all included train events and MUs for an unknown loading data set. As shown in the figure, DIs and DLs were detected with acceptable accuracy for considered MU cases. Observed false positives and negatives had magnitudes that varied with the level of the MU and DL. Ttesting results

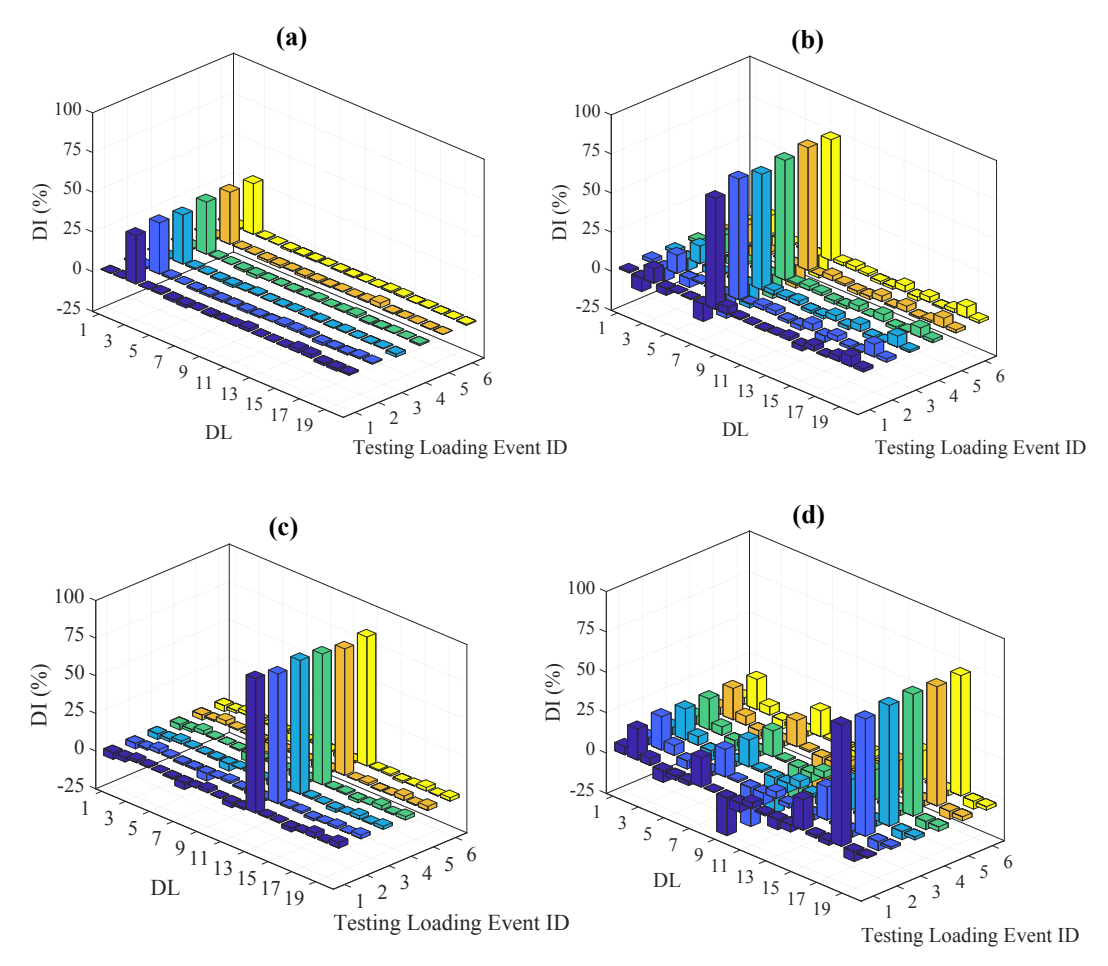


Fig. 18. ANN testing with MU and unknown loading, all testing events: (a) DI 40% at DL 3 with \mathcal{M}_1 ; (b) DI 60% at DL 8 with \mathcal{M}_2 ; (c) DI 80% at DL 13 with \mathcal{M}_4 and (d) DI 100% at DL 18 with \mathcal{M}_5 .

Table 3MU and unknown load testing results.

Figure	Subplot	MU case	Simulated DI and DL	Detected DI at simulated DL	False positive and negative DIs
Fig. 18	a	\mathcal{M}_1	40% at DL 3	30-33%	3%
	b	\mathcal{M}_2	60% at DL 8	71-78%	12 and 15%,
	c	\mathcal{M}_4	80% at DL 13	84-89%	3 and 5%
	d	M_5	100% at DL 18	73-75%	21 and 24%
Fig. 19	a	\mathcal{M}_1	70% at DL 15	61-65%	7 and 10%
	b	\mathcal{M}_2	70% at DL 15	72-82%	6%
	c	\mathcal{M}_4	70% at DL 15	65-70%	17 and 16%
	d	115	70% at DL 15	35-58%	26 and 15%

shown in Fig. 18 are summarized in Table 3.

The influence of MU level on DL and DI detection is illustrated via comparisons for DL 15 and a DI of 70% for all loading events shown in Fig. 19. As shown in the figure, DL and DI detection accuracy vary based on the MU level with false positives and negatives were observed. Summarized results from Fig. 19 are listed in Table 3.

In this section, a numerical investigation was completed to identify a robust damage feature that is largely independent of MU to help generate damage scenarios from measured strains (φ_{exp}). The identified damage feature was $\Delta \varphi_{\mathscr{M}_l}$, which is the difference between healthy and deficient POMs (φ). ANNs were trained and tested based $\Delta \varphi_{\mathscr{M}_l}$ being the damage feature for various MUs and known or unknown loadings. Testing results showed that DL and DI were reasonably detected for different MUs. However, false positives and negatives were observed with magnitudes and locations that varied based on MU and DL. In

general, it can be concluded that MUs with stiffer stringer-to-floor beam end fixity ratios tended to underestimate DIs while MUs cases with more flexible stringer ends tended to overestimate the DI.

5. Field investigation

In this section, measured strains are used to develop φ^h_{exp} considering the studied bridge is currently in a healthy state (i.e., no observed stringer-to-floor beam connection damage). As a result, φ^h_{exp} is dependent on recorded strain signal magnitudes and durations, which are a function of train load, length and speed. To reduce φ^h_{exp} variations associated with train crossing events, data preprocessing was completed to ensure that snapshots used in φ^h_{exp} calculations were of similar magnitude and feature.

Since the identified damage feature $\Delta \varphi_{\mathscr{M}_i}$ was shown to be independent of the MU level largely, a similar correlation was expected between model $\Delta \varphi_{\mathscr{M}_i}$ and field $\Delta \varphi_{exp}$; meaning that both $\Delta \varphi$ should be close to one another. As a result, $\Delta \varphi_{\mathscr{M}_i}$ were used to generate damage scenarios as a function of φ_{exp}^h so that training and testing ANNs using damage scenarios developed from measured strains were possible. A flowchart describing the field investigation procedures is shown in Fig. 20.

5.1. Monitoring system and data collection

Stringer end strains were measured at instrumented locations depicted in Fig. 2 using 20 strain transducers manufactured by Bridge Diagnostics Inc. (BDI). The strain transducer is a waterproof, full Wheatstone bridge with 350 Ω resistance. Transducers are installed by

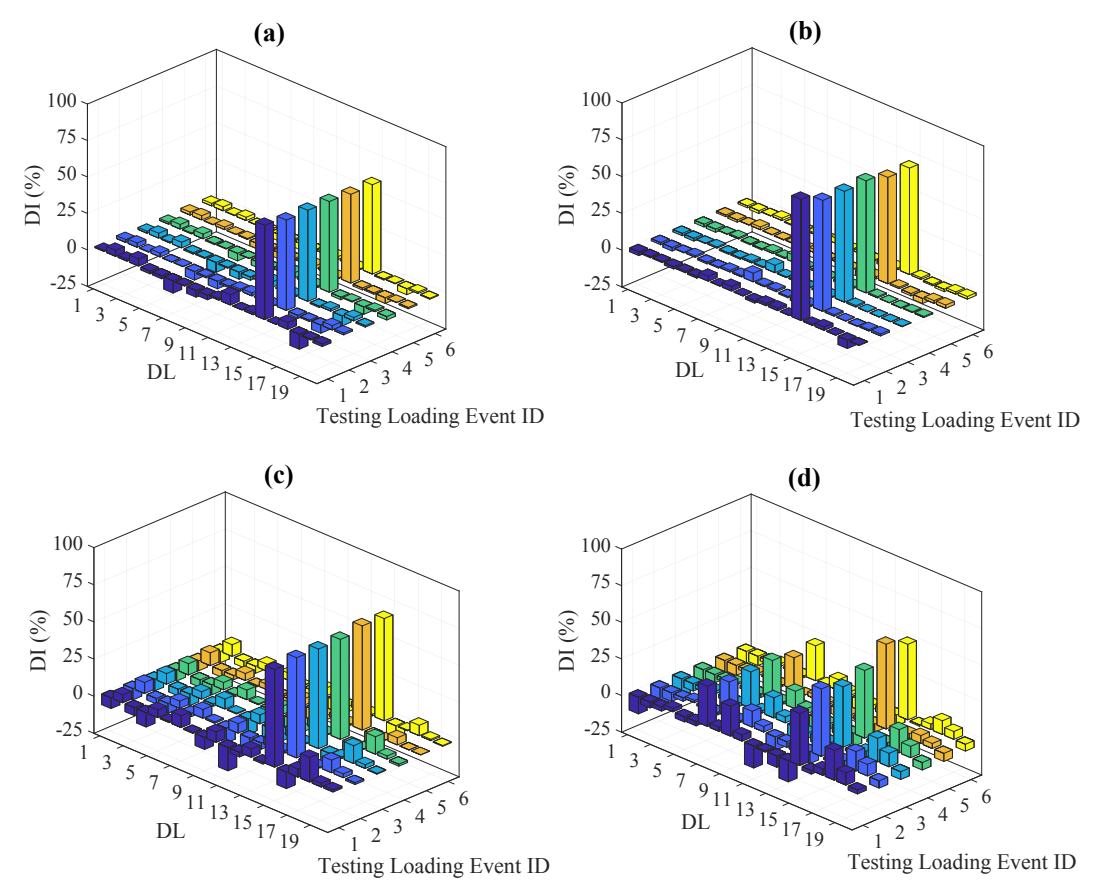


Fig. 19. ANNs testing with MU and unknown loading, DI 70% at DL 15, all testing events: (a) \mathcal{M}_1 ; (b) \mathcal{M}_2 ; (c) \mathcal{M}_4 ; and (d) \mathcal{M}_5 .

preparing the surface of the material and applying adhesive. Strains were recorded when a train crossed the bridge at a sampling rate of 50 Hz. Comparison of measured strain time histories with 50 Hz and 200 Hz sampling rate proved that there was not significant amount of information lost when sampling at 50 Hz. A record event technique was adopted by triggering the strain at ILs 8 and 13 to start recording once their measured strain magnitudes exceeded the predefined value of \pm 5µε. Event recording was set to record strains for a time-window of 4 min. Data preprocessing was completed without prior knowledge of train loads, lengths, location, direction of travel or speed. As a result, loads were non-stationary and unknown.

5.2. Data preprocessing and POM extraction

A total of 2951 train passage events were selected, with strains being collected between June 30 and August 31, 2017. The selection of data processing parameters such as strain magnitudes and signal length was based on trial and error approach to minimize φ_{exp}^h variations and maximize the remained number of training trains. The first preprocessing step involved eliminating time steps before and after train passage. The second step classified signals based on which track was loaded. This yielded a total of 1471 out of the 2951 train events that crossed the bridge on Track 2. Track 2 was the focus of this research work since the bridge is symmetric about its longitudinal axis. More details about the first two preprocessing steps can be found elsewhere [2].

The third step retained signals for similar trains for φ^h_{exp} calculations to reduce loading configuration effects. To reduce φ^h_{exp} variations resulting from differing railroad car numbers and train loads, the first 15 strain peaks from a time-history were automatically selected using recorded strains at location 8 when Track 1 was loaded or location 13 when Track 2 loaded (see Fig. 2). Locations 13 and 18 were selected to be at midspan of the bridge and represented both tracks. Midspan

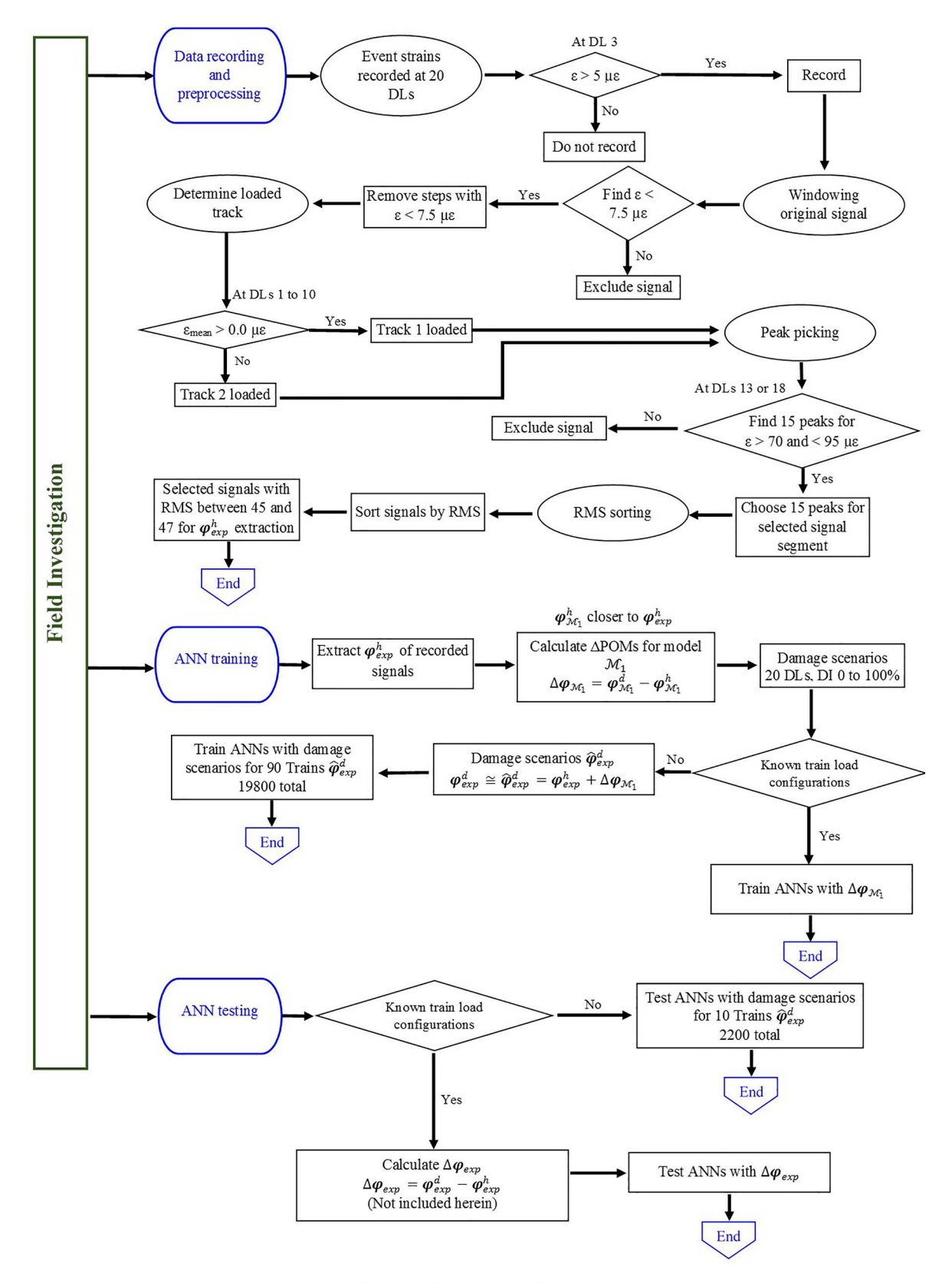
locations were selected to reduce localized, support induced effects on senros readings so that the selected signal time-window start, end and duration would be the same for all sensors. Train events having strain magnitudes greater than 71 µE and less than 95 µE at locations 8 or 13 were retained, which resulted in 195 and 490 train events for Track 1 and Track 2, respectively. The MATLAB findpeaks function was used to select desired strain peaks within defined thresholds. The developed code excluded the first eight peaks out of the 15 that were selected to reduce additional transient variations from locomotive passage. Train speed and axle spacing effects were reduced by selecting signals having a number of time steps greater than 210 and less than 225, which yielded 59 and 172 train events for Track 1 and Track 2, respectively. The thresholds outlined above were determined using a trial and error approach. Since the number of retained train events for Track 2 was higher than those for Track 1, Track 2 results were rack 2 events provided a larger training set and were selected.

The fourth step ensured that the twenty stringer ends in Fig. 2 were subjected to appreciable strains from selected trains. To do so, retained Track 2 strain time-histories were sorted based on average RMS with strain snapshots for RMSs between 44.5 and 47.0 selected having minimal average RMS variation. After performing the fourth step, a total of 100 train events out of the original 1471 events for Track 2 were retained.

The progression of strain signal strain filtering steps at location 13 in Fig. 2 and resulting φ_{exp}^h for Track 2 are shown in Fig. 21. Table 4 provides additional details.

It is observed that strains and φ_{exp}^h for the retained train events show close agreement. Averages of Track 2 strain snapshot matrices RMS values after filtering out loading effects (172 trains events) are shown in Fig. 22 with selected trains highlighted.

It is important to note that changing data processing parameters would change the features and number of retained training and testing



 $\textbf{Fig. 20.} \ \ \textbf{Field investigation flow} \\ \textbf{chart.}$

trains. However, the same criteria should be used for data processing when using the developed framework to assess bridge health. For other bridges, new data processing parameters should be determined from measured responses.

5.3. ANN training and testing data sets

As shown in Fig. 22, selected train IDs were from 62 to 161 with 90 used for ANN training and ten used for testing. Testing IDs were from

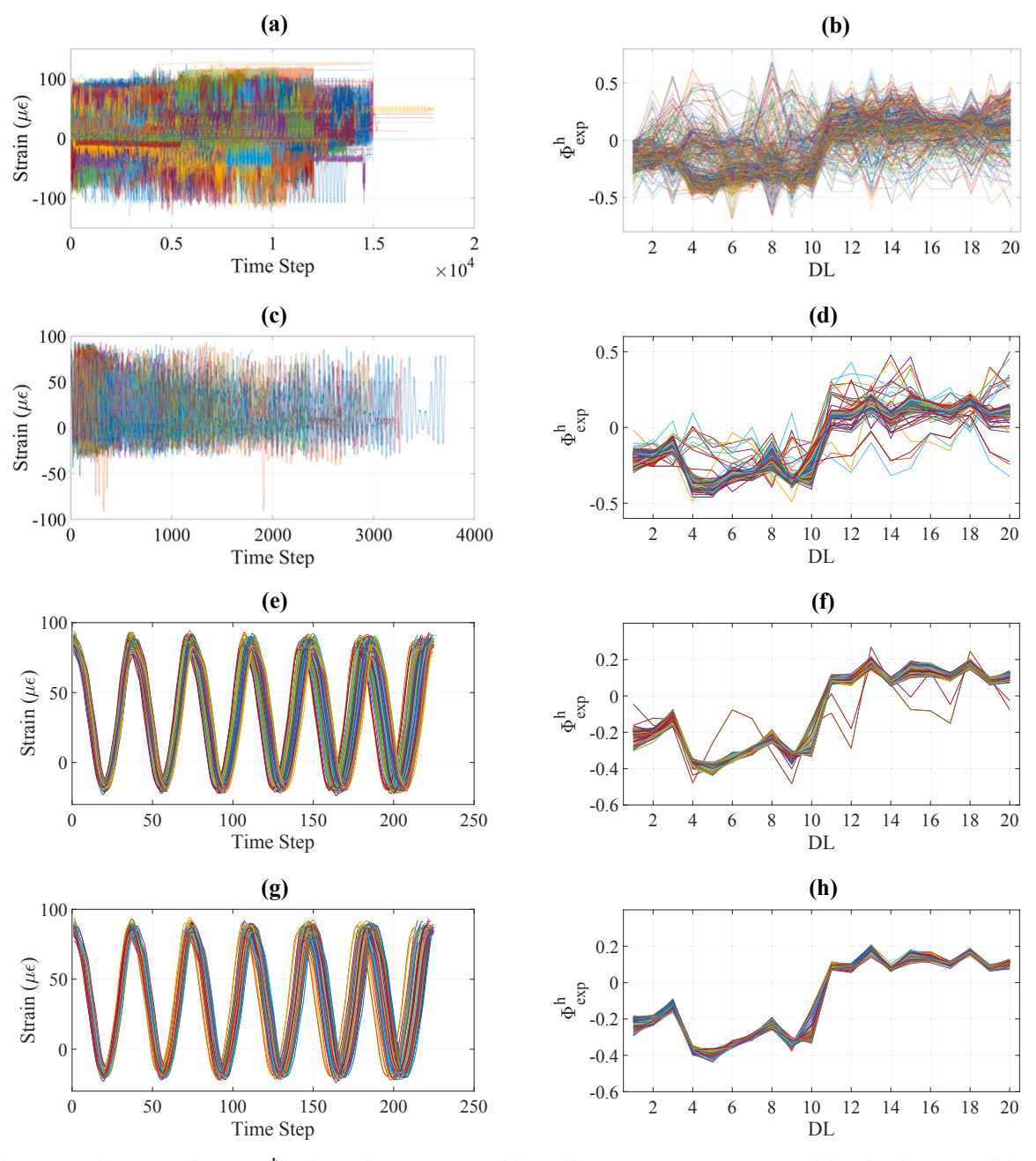


Fig. 21. Track 2 measured strain time-histories φ_{exp}^h values at location 13: (a and b) No filtering, 1471 train events; (c and d) railroad cars, overall length and load magnitude filters applied, 490 events; (e and f) speed and axle spacing filters applied, 172 events; and (g and h) average RMS range filter applied, 100 events.

Table 4Train event preprocessing summary.

Figure	Number of train events	Preprocessing steps
Fig. 21a-b	1471	Trains classified to Track 2
Fig. 21c-d	490	eliminating railroad car number, length and loading effects
Fig. 21e-f	172	eliminating train speed and axle spacing effects
Fig. 21g-h	100	Selected train events after sorting trains by RMS

112 to 121, with average RMS located in the middle of the selected range. Imposing damage to the actual structure was not possible and, as a result, φ^h_{exp} was calculated for the 100 train event strain snapshot matrices and used to develop estimated damage scenarios $(\hat{\varphi}^d_{exp})$ as a function of $\Delta \varphi_{\mathcal{M}_i}$. It is important to reiterate that $\Delta \varphi_{\mathcal{M}_i}$ could be assumed to be very close to $\Delta \varphi_{exp}$. Based on these findings, $\hat{\varphi}^d_{exp}$ was calculated as:

$$\boldsymbol{\varphi}_{exp}^{d} \cong \hat{\boldsymbol{\varphi}}_{exp}^{d} = \boldsymbol{\varphi}_{exp}^{h} + \Delta \boldsymbol{\varphi}_{\mathcal{M}_{1}}$$
(19)

where $\Delta \varphi_{\mathscr{M}_1}$ was selected from considered MU cases because it was shown that $\varphi_{\mathscr{M}_1}^h$ was closer to φ_{exp}^h when compared against the other MU cases as shown in Fig. 23. A set of example comparisons between $\widehat{\varphi}_{exp}^d$ and φ_{exp}^h as shown in Fig. 24 for DIs of 40, 60, 80 and 100% simulated at

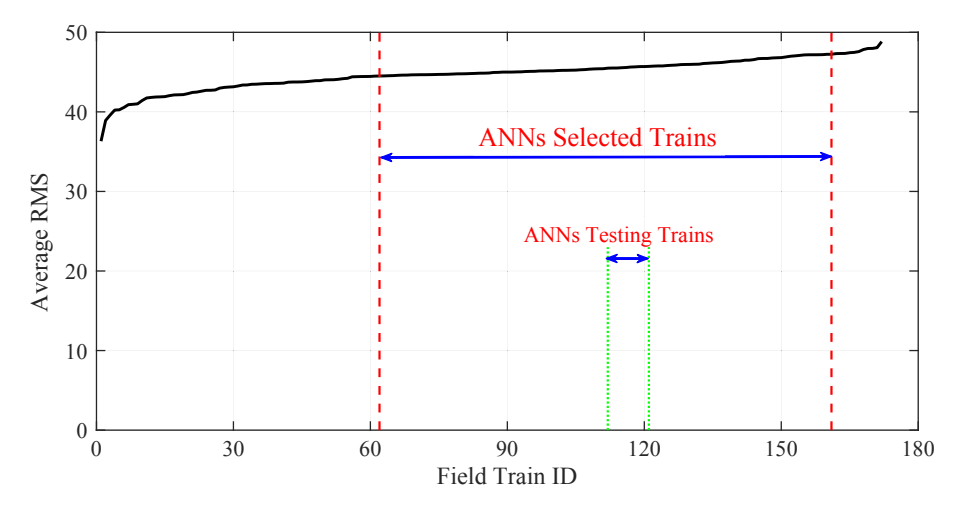


Fig. 22. Strain RMS for Track 2.

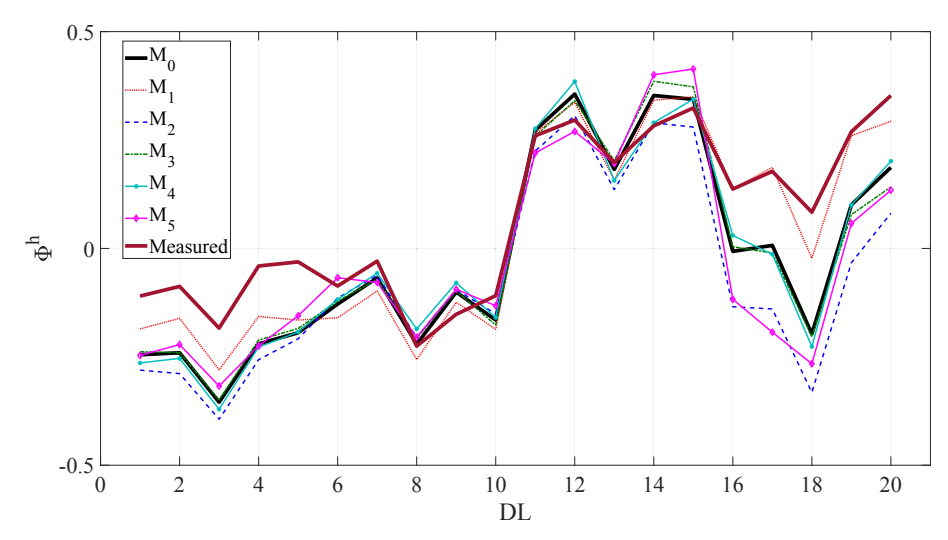


Fig. 23. φ^h mean comparisons, measured and MU cases.

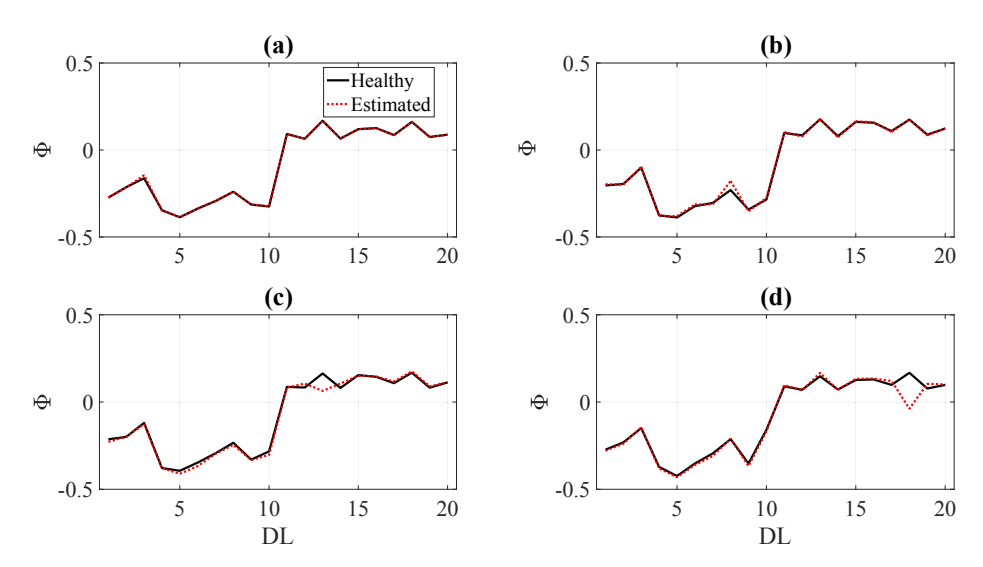


Fig. 24. $\hat{\varphi}^{d}_{exp}$ comparisons to φ^{h}_{exp} for: (a) DI 40% at DL 3, Train 61; (b) DI 60% at DL 8, Train 86; (c) DI 80% at DL 13, Train 111; and (d) DI 100% at DL 18, Train 136.

DL 3, 8, 13 and 18 for trains 61, 86, 111 and 136. The comparison showed significant variation for simulated DLs in $\hat{\varphi}^d_{exp}$ when compared against φ^h_{exp} , with minor variations being observed at other healthy DLs.

The figure also shows that the magnitude of the variation increase as DI increases.

For the 100 train events included in ANN testing and training, a

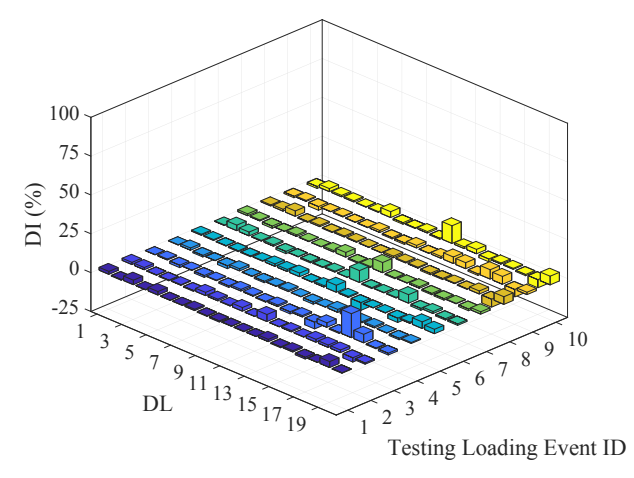


Fig. 25. ANN field testing, all loading events, DI 0%

total of 22,000 damage scenarios were generated using $\Delta \varphi_{\mathcal{M}_1}$, with 19,800 used for training the ANNs. CPU time used for training increased to 4800 min.

5.4. Damage identification results

As mentioned earlier, trains 112 to 121 were arbitrarily selected to validate ANN effectiveness. For the ten observed train events, false positives were between 2 and 15%, which was considered low when compared to the DI of 0%. See Fig. 25.

ANN testing for DIs of 40, 60, 80 and 100% at DL 3, 8, 13 and 18 are shown in Fig. 26 for all selected events. DI and DL were detected with acceptable accuracy for considered damage scenarios and testing events; however, detected DI accuracy and the numbers of false

Table 5Field testing results.

Figure	Simulated DI and DL	Detected DI at simulated DL	False positive and negative DIs
Fig. 26a	40% at DL 3	17–43%	32%
Fig. 26b	60% at DL 8	49–70%	11 and 15%
Fig. 26c	80% at DL 13	74–82%	12 and 10%
Fig. 26d	100% at DL 18	100–102%	10 and 13%

positives varied based on DL and DI. It was observed that false-positive existence and magnitudes increased with lower DI and reduced as DI increased. The results shown in Fig. 26 are summarized in Table 5.

In this section, a field investigation was completed that involved preprocessing measured strains to reduce φ_{exp}^h variations associated with variations in loading configurations, training, and testing the ANNs with damage scenarios generated from φ_{exp}^h and $\Delta \varphi_{\mathscr{M}_1}$. The results showed that DI and DL were detected with acceptable accuracy under the included field loading events.

6. Conclusions

Stringer-to-floor beam connections are known to be fatigue prone details in riveted, steel, railway bridges. Preemptively detecting potential fatigue damage is of significant interest to railway bridge owners to prevent future deficiencies that could lead to safety concerns and traffic interruptions. SHM has been used by bridge owners to establish structural health with researchers studying model-based and data-based SHM frameworks to locate potential fatigue prone zones via detecting changes in bridge behavior.

To advance SHM state-of-the-art associated with detecting and characterizing potential fatigue prone locations on a double-track, steel, riveted truss, railway bridge, an output-only, automated, damage

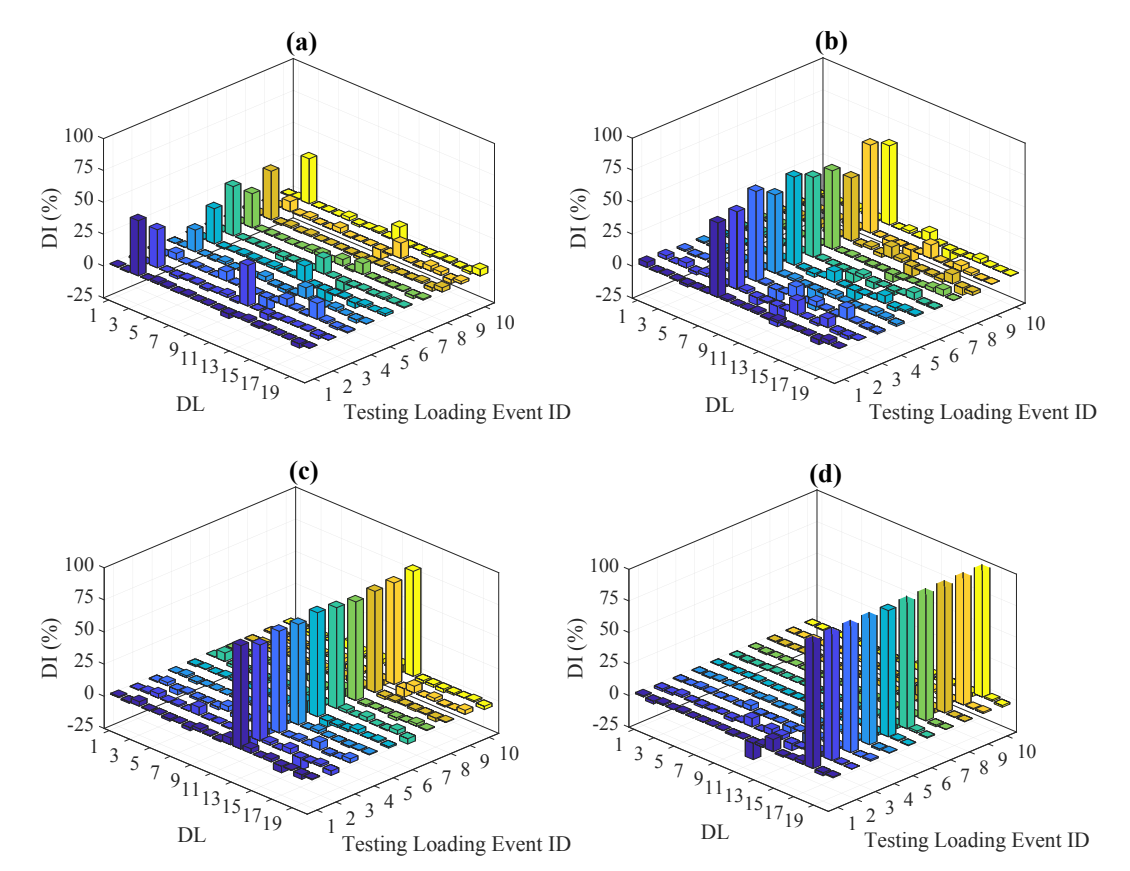


Fig. 26. ANN field testing, all testing events: (a) DI 40% at DL 3; (b) DI 60% at DL 8; (c) DI 80% at DL 13; and (d) DI 100% at DL 18.

detection framework based on recorded strains and using POD and ANNs as previously proposed by the authors [1,2]. The current study uses a hybrid experimental-numerical approach to improve the framework further so that it can maintain damage detection accuracy in the presence of modeling uncertainties. The numerical portion of the study identified a damage feature, $\Delta \varphi$, that is largely independent of MU level. While the identified feature was quite robust, it was observed that damage detection accuracy reduced as the level of the assumed MU increased.

The experimental portion of the study generated damage scenarios based on $\Delta\varphi_{\mathscr{M}_1}$ to train ANNs under the passage of 90 train events over an in-situ bridge whose strain response was measured. Developed ANNs were tested under an additional ten train events. Acceptable DI and DL detection was observed, with DI detection accuracy increasing as simulated DI increased. The magnitude and existence of false positives were also influenced by DI and DL, with a higher number and magnitudes of false positives observed for lower DIs.

It is important to note that, when MU is considered, and if measuring train loadings and configurations are possible, $\Delta \varphi$ should be used to train and test the developed POD-ANN framework to improve its damage detection accuracy. When measuring loading configuration is challenging, $\hat{\varphi}^d_{exp}$ (i.e., estimated damage scenario POMs based on field measurements) should be used to train and test the framework with lower damage detection accuracy being expected when compared against the known loading scenario.

Ongoing work includes:

- Considering environmental variability to improve the framework and further eliminate false alarms;
- Determining damage thresholds from statistical investigations; and
- Imposing damage scenarios on the studied bridge to evaluate the correlation between numerical and experimental Δφ.

Declaration of Competing Interest

The authors declare that they have no known competing financial interests or personal relationships that could have appeared to influence the work reported in this paper.

Acknowledgments

The authors would like to acknowledge the support provided by NSF Award #1636805 BD Spokes, Planning, Midwest: Big Data Innovations for Bridge Health. The authors also gratefully acknowledge assistance provided by the University of Nebraska-Lincoln Holland Computing Center, Union Pacific and Bridge Diagnostics Inc. in association with this project.

Appendix A. Supplementary material

Supplementary data to this article can be found online at https://doi.org/10.1016/j.ijfatigue.2019.105458.

References

- [1] Eftekhar Azam Saeed, Rageh Ahmed, Linzell Daniel. Damage detection in structural systems utilizing artificial neural networks and proper orthogonal decomposition. Struct Control Health Monit 2019;26(2):e2288. https://doi.org/10.1002/stc.v26. 210.1002/stc.2288.
- [2] Rageh A, Linzell DG, Azam SE. Automated, strain-based, output-only bridge damage detection. J Civil Struct Health Monitor 2018;8(5):833–46.
- [3] Rakoczy AM. Development of system reliability models for railway bridges. The University of Nebraska-Lincoln; 2012.
- [4] Haghani R, Al-Emrani M, Heshmati M. Fatigue-prone details in steel bridges. Buildings 2012;2(4):456–76.
- [5] Rageh A, Linzell D. Optimized health monitoring plans for a steel, double-track railway bridge [dissertation] University of Nebraska-Lincoln; 2018.
- [6] Imam B, Righiniotis TD, Chryssanthopoulos MK. Fatigue assessment of riveted railway bridges. Steel Struct 2005;5(5):485–94.

- [7] Al-Emrani M. Fatigue performance of stringer-to-floor-beam connections in riveted railway bridges. J Bridge Eng 2005 Mar;10(2):179–85.
- [8] Al-Emrani M, Akesson B, Kliger R. Overlooked secondary effects in open-deck truss bridges. Struct Eng Int 2004;14(4):307–12.
- [9] Chotickai P, Kanchanalai T. Field testing and performance evaluation of a throughplate girder railway bridge. Transp Res Rec: J Transp Res Board 2010;2172:132–41.
- [10] Imam B, Righiniotis TD, Chryssanthopoulos MK. Connection fixity effects on stress histories in riveted rail bridges. Bridge maintenance, safety, management and cost; 2004.
- [11] Spyrakos CC, Raftoyiannis IG, Ermopoulos JC. Condition assessment and retrofit of a historic steel-truss railway bridge. J Constr Steel Res 2004;60(8):1213–25.
- [12] Tobias DH, Foutch DH, Choros J. Investigation of an open deck through-truss railway. Bridge: Work Train Tests 1993.
- [13] Phares BM, Rolander DD, Graybeal BA, Washer GA. Reliability of visual bridge inspection. Public Roads 2001;64(5).
- [14] Farrar CR, Worden K. Structural health monitoring: a machine learning perspective. John Wiley & Sons; 2012.
- [15] Achenbach JD. Structural health monitoring-what is the prescription? Mech Res Commun 2009;36(2):137–42.
- [16] Glisic B, Inaudi D. Development of method for in-service crack detection based on distributed fiber optic sensors. Struct Health Monitor 2012;11(2):161–71.
- [17] Harmanci YE, Spiridonakos MD, Chatzi EN, Kübler W. An autonomous strain-based structural monitoring framework for life-cycle analysis of a novel structure. Front Built Environ 2016;2:13.
- [18] Glisic B, Inaudi D. Fibre optic methods for structural health monitoring. John Wiley & Sons; 2008.
- [19] Shokrani Y, Dertimanis VK, Chatzi EN, Savoia NM. On the use of mode shape curvatures for damage localization under varying environmental conditions. Struct Control Health Monitor 2018.
- [20] Tan ZX, Thambiratnam DP, Chan T, Razak HA. Detecting damage in steel beams using modal strain energy based damage index and Artificial Neural Network. Eng Failure Anal 2017;79:253–62.
- [21] Ashory M, Ghasemi-Ghalebahman A, Kokabi M. An efficient modal strain energy-based damage detection for laminated composite plates. Adv Compos Mater 2017:1–16.
- [22] Moaveni B, He X, Conte JP, Restrepo JI. Damage identification study of a sevenstory full-scale building slice tested on the UCSD-NEES shake table. Struct Saf 2010;32(5):347–56.
- [23] Taciroglu E, Ghahari SF, Abazarsa F. Efficient model updating of a multi-story frame and its foundation stiffness from earthquake records using a timoshenko beam model. Soil Dyn Earthquake Eng 2017;92:25–35.
- [24] Bellino A, Fasana A, Garibaldi L, Marchesiello S. PCA-based detection of damage in time-varying systems. Mech Syst Sig Process 2010;24(7):2250–60.
- [25] Thiene M, Galvanetto U. Impact location in composite plates using proper orthogonal decomposition. Mech Res Commun 2015;64:1–7.
- [26] Kim Y, Eun H. Comparison of damage detection methods depending on FRFs within specified frequency ranges. Adv Mater Sci Eng 2017;2017.
- [27] O'Connor SM, Zhang Y, Lynch JP, Ettouney MM, Jansson PO. Long-term performance assessment of the Telegraph Road Bridge using a permanent wireless monitoring system and automated statistical process control analytics. Struct Infrastruct Eng 2017;13(5):604–24.
- [28] Dervilis N, Choi M, Taylor SG, Barthorpe RJ, Park G, Farrar CR, et al. On damage diagnosis for a wind turbine blade using pattern recognition. J Sound Vibrat 2014;333(6):1833–50.
- [29] Ou Y, Chatzi EN, Dertimanis VK, Spiridonakos MD. Vibration-based experimental damage detection of a small-scale wind turbine blade. Struct Health Monitor 2017;16(1):79–96.
- [30] Behmanesh I, Moaveni B, Papadimitriou C. Probabilistic damage identification of a designed 9-story building using modal data in the presence of modeling errors. Eng Struct 2017;131:542–52.
- [31] Law SS, Li XY, Lu ZR. Structural damage detection from wavelet coefficient sensitivity with model errors. J Eng Mech 2006;132(10):1077–87.
- [32] Moaveni B, He X, Conte JP, Restrepo JI, Panagiotou M. System identification study of a 7-story full-scale building slice tested on the UCSD-NEES shake table. J Struct Eng 2010;137(6):705–17.
- [33] Moaveni B, Barbosa AR, Conte JP, Hemez FM. Uncertainty analysis of system identification results obtained for a seven-story building slice tested on the UCSD-NEES shake table. Struct Control Health Monitor 2014;21(4):466–83.
- [34] Astroza R, Alessandri A. Effects of model uncertainty in nonlinear structural finite element model updating by numerical simulation of building structures. Struct Control Health Monitor 2019;26(3):e2297.
- [35] Chatzi EN, Smyth AW, Masri SF. Experimental application of on-line parametric identification for nonlinear hysteretic systems with model uncertainty. Struct Saf 2010;32(5):326–37.
- [36] Lee JJ, Lee JW, Yi JH, Yun CB, Jung HY. Neural networks-based damage detection for bridges considering errors in baseline finite element models. J Sound Vibrat 2005;280(3–5):555–78.
- [37] Astroza R, Alessandri A, Conte JP. A dual adaptive filtering approach for nonlinear finite element model updating accounting for modeling uncertainty. Mech Syst Sig Process 2019;115:782–800.
- [38] Pearson KLIII. On lines and planes of closest fit to systems of points in space. London, Edinburgh, Dublin Philos Mag J Sci 1901;2(11):559–72.
- [39] Karhunen K. Über lineare Methoden in der Wahrscheinlichkeitsrechnung. Sana; 1947.
- [40] Klema V, Laub A. The singular value decomposition: Its computation and some applications. IEEE Trans Autom Control 1980;25(2):164–76.

- [41] Liang YC, Lee HP, Lim SP, Lin WZ, Lee KH, Wu CG. Proper orthogonal decomposition and its applications—Part I: Theory. J Sound Vibrat 2002;252(3):527–44.
- [42] Dworakowski Z, Dragan K, Stepinski T. Artificial neural network ensembles for fatigue damage detection in aircraft. J Intell Mater Syst Struct 2017;28(7):851–61.
- [43] Gu J, Gul M, Wu X. Damage detection under varying temperature using artificial neural networks. Struct Control Health Monitor 2017;24(11):e1998.
- [44] Amezquita-Sanchez JP, Adeli H. Feature extraction and classification techniques for health monitoring of structures. Scientia Iranica. Trans A Civ Eng 2015;22(6):1931.
- [45] Irie B, Miyake S. Capabilities of three-layered perceptrons. IEEE International Conference on Neural Networks; 1988.
- [46] Nguyen D, Widrow B. Improving the learning speed of 2-layer neural networks by choosing initial values of the adaptive weights. In: International joint conference on neural networks, 1990. 1990 IJCNN. IEEE; 1990.
- [47] Bishop CM. Pattern Recognition and Machine Learning. Springer; 2006.
- [48] MacKay DJ. Bayesian interpolation. Neural Comput 1992;4(3):415-47.
- [49] Cybenko G. Approximation by superpositions of a sigmoidal function. Math Control Signals Syst 1989;2(4):303–14.
- [50] Schmidhuber J. Deep learning in neural networks: an overview. Neural Networks 2015;61:85–117.
- [51] Waszczyszyn Z. Fundamentals of artificial neural networks. Neural networks in the analysis and design of structures. Springer; 1999. p. 1–51.
- [52] Foresee FD, Hagan MT. Gauss-Newton approximation to Bayesian learning. IEEE;
- [53] Moler C, Little J, Bangert S. Matlab user's guide-the language of technical computing. Sherborn, Mass: The MathWorks; 2001.